Arab J Geosci (2015) 8:8399–8418
DOI 10.1007/s12517-015-1813-8

ORIGINAL PAPER

Geology, geochemistry, and some genetic discussion of the Chador-Malu iron oxide-apatite deposit, Bafq District, Central Iran

Armin Sabet-Mobarhan-Talab · Firouz Alinia · Seyyed-Saeed Ghannadpour · Ardeshir Hezarkhani

Received: 19 September 2014 / Accepted: 20 January 2015 / Published online: 4 February 2015

Abstract The Chador-Malu iron oxide-apatite system (Bafq District, Central Iran) contains the largest known iron ore deposit in Iran (pre-mining reserve of 400 Mt @ 55 % Fe), and comprises the pipe-like northern (this study) and the sill-like southern orebodies of predominantly massive ore, and a sodic-calcic alteration envelope. The geology and geochemistry of the Chador-Malu deposit demonstrates its similar characteristics to the Kiruna-type deposits. There is circumstantial evidence for rare earth elements (REE) mobilization during apatite leaching by high-temperature fluids and associated monazite nucleation. Pervasive actinolitization of the rhyolitic country rocks led to the formation of actinolite-rich metasomatic host rocks, which represent another evidence for high-temperature fluids at Chador-Malu. Hydrothermal mineralization is suggested by small iron ore veins (2–3 cm thick) and breccias cemented by iron oxides, as well as a Fe-metasomatism which overprints all types of host rock alteration. Based on REE geochemistry and spatial relationships, it is proposed that a potential source for metals and P could be late-stage Fe-P melt differentiates of the Cambrian magmatism, which is consistent with the late Fe-metasomatism of the host rocks. The proposed Fe-P melts and the mineralization would be linked by hydrothermal media through the zones of ring fracture at Chador-Malu and similar parts of the Bafq district.

Keywords Bafq · Ferride geochemistry · REE geochemistry · Metasomatism · Fe-P melt

A. Sabet-Mobarhan-Talab (✉) · F. Alinia · S.-S. Ghannadpour · A. Hezarkhani
Department of Mining and Metallurgical Engineering, Amirkabir University of Technology (Tehran Polytechnic), 424 Hafez Ave., Tehran 15916-34311, Iran
e-mail: armin.sabet@aut.ac.ir

Introduction

Iron oxide-apatite and iron oxide-copper-gold (IOCG) deposits are an important group of economic iron oxide-rich deposits in the world. Some of the well-known districts containing such deposits are northern and central Sweden (Kiruna-type deposits), the Andean Coastal Batholith in Chile and Peru (an example of a paired barren iron oxide-apatite/productive IOCG belt), the El Laco Volcanic Complex in Chile, and the Bafq district, Central Iran, hosting the Chador-Malu deposit.

The Kiruna-type iron oxide-apatite and IOCG deposits may be considered to form the end-members of a continuum of deposit types within one broad class (Hitzman et al. 1992). A common feature that the two end-members share is intracontinental extensional tectonics (Hitzman 2000); however, some districts are associated with orogenic collapse (Duncan et al. 2014). There are also examples of IOCG mineralization associated with porphyry copper deposits in subduction zones (e.g., in the Yerington district, Nevada; see Groves et al. 2010). The iron oxide-apatite deposits of different age and geological settings show remarkably similar alteration and mineralization style, whereas the IOCG deposits are more diverse. While the two end-members may have fundamentally different origins (Hitzman 2000), the presence of both iron oxide-apatite and IOCG systems in the same mineralized belts can suggest their similar genesis, but with different local-scale processes and/or sources.

The genesis of Kiruna-type deposits has been subject to substantial controversy. There is generally close spatial association between Kiruna-type deposits and igneous rocks, the composition and depth of the latter ranging from mafic to felsic and intrusive to volcanic, respectively. There is, however, no consensus among researchers as to the principal source

of the fluids possibly responsible for mineralization or the nature of the contribution of associated magmas (e.g., Parak 1975; Hildebrand 1986; Frietsch and Perdahl 1995; Barton and Johnson 1996, 2004; Broman et al. 1999; Sillitoe and Burrows 2002; Williams et al. 2005). Researchers put forward two different genetic models involving magmatic (e.g., Frietsch 1978, 1984; Nyström and Henriquez 1994; Naslund et al. 2002; Jonsson et al. 2013) and hydrothermal processes (e.g., Hitzman et al. 1992; Rhodes and Oreskes 1999; Hitzman 2000; Barton and Johnson 2000; Daliran 2002; Daliran et al. 2007; Smith et al. 2013).

Some researchers have proposed an IOCG affinity for the Bafq district deposits (see, e.g., Daliran 2002; Torab and Lehmann 2007; Torab 2008; Stosch et al. 2011), after the class was defined by Hitzman et al. (1992). Evidence for an IOCG association includes the presence of hydrothermal alteration with the characteristic zoning of the IOCG deposits (as defined by Hitzman et al. 1992) and magnetite chemistry (e.g., Torab 2008).

Jami (2005) developed a three-stage model for the hydrothermal evolution of the Esfordi deposit based on apatite textures, fluid inclusions, and isotopic data; however, the initial stages in the generation of the proto iron oxide-apatite body was largely speculative and involved the immiscible separation of a Fe-P melt (in response to a possible magma mingling in the Esfordi area) and its subsequent equilibration with fluids near 400 °C (see also Jami et al. 2007). From a regional perspective, Torab (2008) considered the evaporites of Central Iran as ligand source for metal leaching and transport (as described by Barton and Johnson 1996), and based on Nd isotopic data proposed that the rare earth elements (REE) and P of the Bafq district deposits were remobilized from phosphorites (which are not documented in the Early Cambrian sedimentary sequence of Central Iran, but are present in the stratigraphically equivalent formations outside the region) and were supplied, to a lesser degree, from the leaching of igneous rocks (see also Torab and Lehmann 2007). They, however, did not discuss the source of such large amounts of iron oxide in the Bafq district. A source for Fe proposed by some researchers has been the pre-existing mafic minerals (iron-bearing amphibole and pyroxene) of the Precambrian rocks of the region which would decompose in the early stages of regional-scale hydrothermal fluid circulation to supply Fe to the system (e.g., Haghipour 1974; Daliran et al. 2007, 2010).

Based principally on flow and quenching textures observed in magnetite, liquid magmatic models have been ascribed a prominent role at Kiruna and El Laco (see, e.g., Foose, and Mclelland 1995; Henriquez and Nyström 1998). This textural evidence was reported from Chador-Malu and certain other Bafq district deposits and interpreted as their direct magmatic origin by Förster and Jafarzadeh (1994). Magmatic models involving immiscibility between silicate and iron oxide-rich melts have widely been proposed for the genesis of Kiruna-type deposits (e.g., Philpotts 1967, 1982; Frietsch 1978, 1984; Naslund et al. 2000). Similar models have been developed for the Bafq district iron oxide-apatite deposits including Chador-Malu (e.g., Williams and Houshmand-Zadeh 1996; Förster and Borumandi 1971; Förster and Jafarzadeh 1984; Jami 2005). Interpreting magnetite lava flows and magnetite-bearing pyroclastic rocks at Chador-Malu, the latter researches supported an immiscible liquid magmatic model of formation, and suggested a carbonatitic affinity for the ore melt based on textural evidence such as xenomorphic calcite and dolomite in the grain boundaries of magnetite, and the absence of relicts of pre-existing carbonates within magnetite grains. However, the later work by Förster and Jafarzadeh (1994) considered the discordant magnetite bodies of the Bafq district, particularly the Chador-Malu deposit, the product of crystallization from an immiscible Fe ± P melt differentiated from an upper mantle carbonated melanephelinitic magma.

Bafq district deposits, of which Chador-Malu is typical, are remarkably similar to the Kiruna-type iron oxide-apatite deposits, considering their mineralogy and associated regional aprons of high temperature sodic-calcic alteration minerals. They consist of massive to brecciated, elongated, and conformable lenses of magnetite-hematite-apatite, which are mainly hosted in felsic volcanics and volcano-sedimentary rocks (e.g., NISCO 1980; Daliran 1990, 2002; Förster and Jafarzadeh 1994; Bonyadi et al. 2011), very similar to the classic Kiirunavaara deposit (northern Sweden), in terms of morphology, ore mineralogy, and host lithology; the latter ranging in composition from felsic to intermediate for the Swedish counterpart (e.g., Hitzman 2000). The volcanic hosts of both districts (Bafq and Kiruna) have undergone intense alteration and formed similar assemblages including actinolite and albite (e.g., Hitzman 2000; Jami 2005; Torab 2008; Bonyadi et al. 2011; Sabet-Mobarhan-Talab 2014).

There is discussion relating Esfordi and Se-Chahun iron oxide-apatite deposits (Bafq District) to the Rapitan-type banded iron-phosphorus formations based on the presence of keratophyres, jaspilites, diamictites, dropstones, and apatite geochemistry (e.g., Aftabi et al. 2009; Mohseni and Aftabi 2012). There have also been other works suggesting a carbonatitic affinity for apatites of the Bafq district deposits based on mineralogical and geochemical studies (e.g., Daliran 2002; Darvishzadeh 1983; Darvishzadeh and Aletaha-Kohbanani 1996).

Although the Chador-Malu deposit is the largest in the Bafq district (400 Mt @ 55 % Fe), it has received the least previous attention to its geochemical characteristics. This paper describes aspects of the geology and geochemistry of this iron oxide-apatite deposit and discusses a possible link between the Cambrian plutonic rocks and mineralization.

Geological setting

The Chador-Malu iron oxide-apatite deposit is located in the Bafq district, which is part of the Central Iranian microplate in the Alpine-Himalayan orogenic system. A series of intersecting regional-scale faults divide the Central Iranian Terrane into three major crustal domains, namely the Lut, Tabas, and Yazd Blocks, among which lies a more than 1, 000-km long, and up to 80 km wide, arcuate and structurally complex belt, called the Kashmar-Kerman volcano-plutonic arc (Ramezani and Tucker 2003), which hosts the Bafq district and the Early Cambrian volcanic and plutonic rocks of Central Iran (Fig. 1).

A model proposed for the Early Cambrian tectonics and magmatism in the Bafq district is crustal extension associated with intracontinental rifting. It has been proposed that this rifting event formed an aborted rift associated with alkaline magmatism, including alkaline volcanic rocks, alkaline granites, and carbonatites (e.g., Samani 1988, 1998; Daliran 1990, 1999, 2002; Förster and Jafarzadeh 1994). However, attributing the regional-scale arcuate faults of the Bafq district (Fig. 1) to a back-arc extensional setting, Ramezani and Tucker (2003) suggested that the Kashmar-Kerman volcano-plutonic arc represents an active continental-margin environment in relation to subduction under the Central Iranian microplate and closure of a Proto-Tethys ocean in the Early Cambrian.

The Early Cambrian sequence in Central Iran consists of a complex set of volcano-sedimentary rocks which extends from Poshte-Badam to Zarand and hosts the most important iron oxide-apatite, Pb-Zn, and U ore deposits in Iran (Samani 1988) (Fig. 1). The volcanic rocks vary from felsic to mafic in composition and include rhyolite, agglomeratic tuff, splitic lava, and diabase, but dominantly rhyolitic rocks, most of which having been subject to widespread alkaline metasomatism (K-feldsparization and albitization; e.g., Daliran et al. 2007). The sedimentary rocks consist of dolomites, dolomitic limestones, and evaporites (Torab 2008). Ramezani and Tucker (2003) assigned an Early Cambrian age (529–554 Ma) for the volcanic suites of this volcano-sedimentary unit and named this sequential unit as Cambrian Volcano Sedimentary Unit (CVSU).

Intruded into the CVSU, as well as into the Upper Precambrian metamorphic rocks, are plutonic bodies of mostly granitic composition (locally associated with diorite and gabbro-diorite dikes or sills), which are quite common in Central Iran, of which the Zarigan, Narigan, and the Chador-Malu granites are located in the Bafq district (Fig. 2). Based mainly on their high sodium contents, Berberian and Berberian (1981)

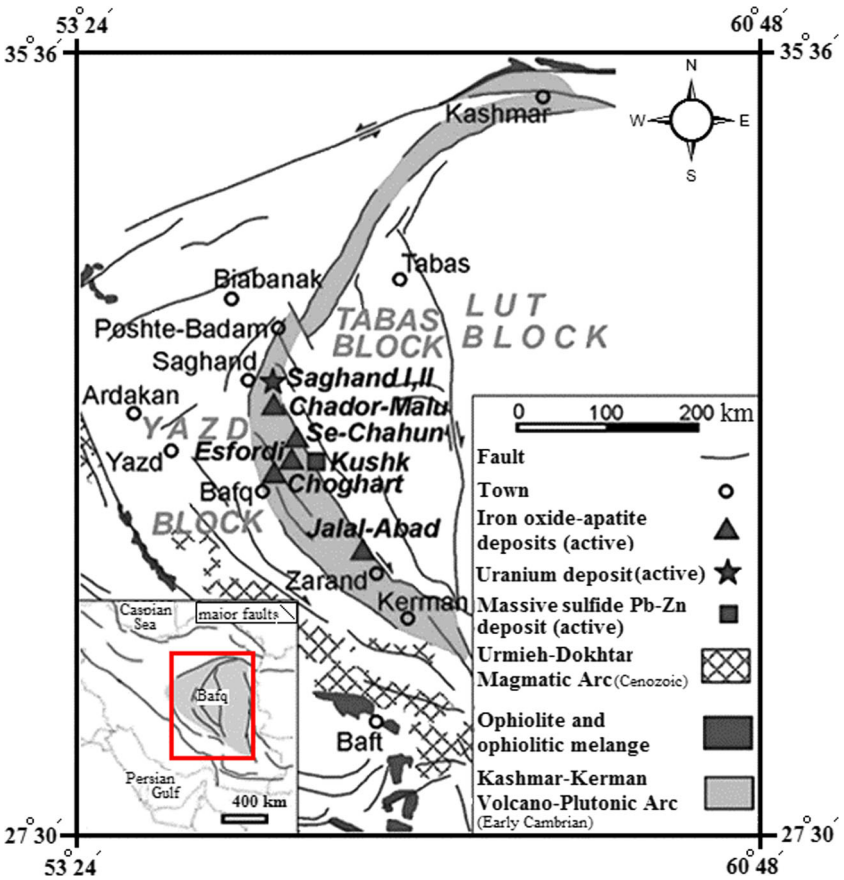

Fig. 1 Structural map of eastern Central Iran (modified after Ramezani and Tucker 2003; Torab 2008). The arcuate Kashmar-Kerman volcano-plutonic arc encompasses the Bafq district which covers the area between Bafq and Saghand and hosts the most important iron oxide-apatite deposits

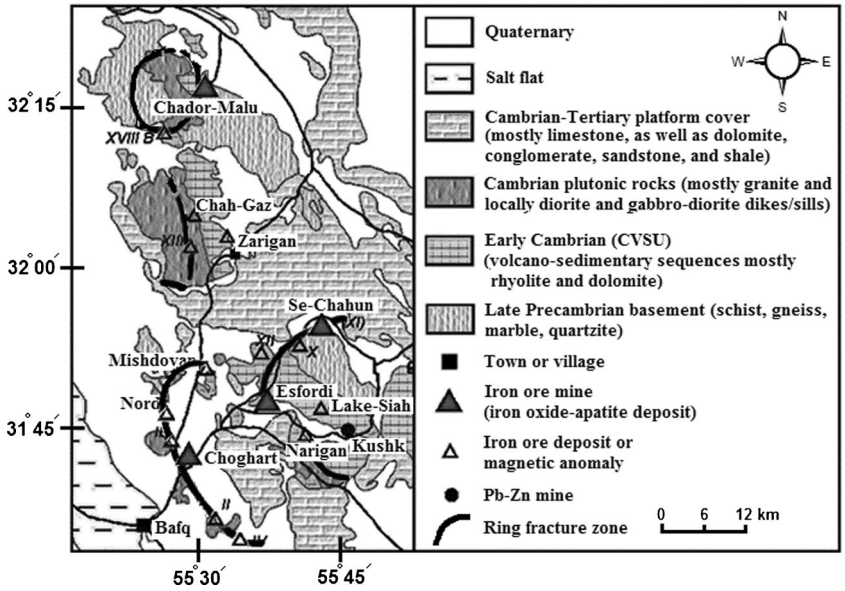

Fig. 2 Simplified geological map of the Bafq district (modified after Förster and Jafarzadeh 1994; Moghtaderi et al. 2007; Torab 2008). Note the spatial relationship between the Chador-Malu deposit and the Cambrian plutonic rocks (Chador-Malu granite)

described these granitic intrusions as alkali granite. The same was considered by later researchers (e.g., Samani 1988; Förster and Jafarzadeh 1994; Daliran 2002; Ghorbani 2013); however, Torab (2008) contends that these rocks are calc-alkaline intrusions affected by widespread sodic alteration (albitization), and suggests an evaporitic source for Na. Both the Zarigan and the Chador-Malu granites are characterized by being conspicuously lacking in mafic minerals (Torab 2008), the latter consisting of orthoclase (51 %), quartz (32 %), plagioclase (14.3 %), and accessory minerals such as zircon, garnet, and titanite (Berberian and Berberian 1981). Ramezani and Tucker (2003) defined an age of 525±7 Ma and 529±16 Ma (U-Pb on zircon) for the Zarigan and the Chador-Malu granites, respectively. Stosch et al. (2011) determined the U-Pb apatite age for major iron oxide-apatite deposits in the Bafq district (527–539 Ma). These ages fell entirely within the age range of the felsic plutonic rocks of the Bafq district (including those mentioned above) dated by Ramezani and Tucker (2003) (525–547 Ma; U-Pb on zircon).

Chador-Malu is among the Bafq district iron oxide-apatite deposits which have been described as iron oxide melt-filled volcanic vents, a morphological feature interpreted as its magmatic origin (e.g., Jafarzadeh 1981; Förster and Jafarzadeh 1984, 1994). The oxygen isotopic composition ($\delta^{18}O$) of iron oxides from the Chador-Malu deposit (−0.64 to 2.19 ‰; Shamsi-Pour et al. 2008) is also consistent with magma as their direct or indirect source. The northern orebody (this study; Figs. 3 and 4a) has the shape of an upright cylinder with several horizontal extensions and is more than 600 m deep. The southern orebody is a flat-lying lens, interpreted as magnetite lava flow or sill. These two orebodies accompanied by two other magnetic anomalies in the Chador-Malu area are arranged in north-northeast-south-southwest direction along the eastern segment of the ring fracture zone shown in Fig. 2 (Förster and Jafarzadeh 1994).

According to field observations, the main host rock of the northern orebody is a highly altered actinolite-rich CVSU rhyolite, documented under the name "metasomatite" (Moghtaderi et al. 2007), and locally known as "Green Rock" (Jami 2005; Torab 2008), which displays sharp contacts with the massive orebody (see the next section). Comprising the main host rock of major iron oxide-apatite deposits in the Bafq district (see, e.g., Jami 2005; Torab 2008; Bonyadi et al. 2011), this metasomatic rock is widespread in the region and is thought to be the consequence of a multistage regional metasomatism (Daliran et al. 2007) in relation to the intrusion of the Cambrian plutonic rocks.

Ore types, mineralogy, and host rock alterations

Mineralization at Chador-Malu occurs predominantly within the actinolite-rich metasomatic rocks and rhyolites (Fig. 3), and comprises the northern pipe-like (this study) and the southern sill-like orebodies. The northern orebody, which is currently subject to extensive mining activity (Fig. 4a), is characterized chiefly by massive mineralization style. This orebody shows sharp and linear contacts with the host rocks (Fig. 4b). The contact between the diorites and either rhyolites or metasomatites (Fig. 3) is largely obscured by hydrothermal alteration and sharp contacts are restricted to structurally controlled zones. Breccias with iron oxide cement as well as small ore veins are rare. The iron ore veins are usually 2–3 cm thick, and can be observed at the contact between the massive ore and host rocks (Fig. 5a). The breccias consist of angular fragments of the metasomatic host rock cemented by iron ore (Fig. 5b)

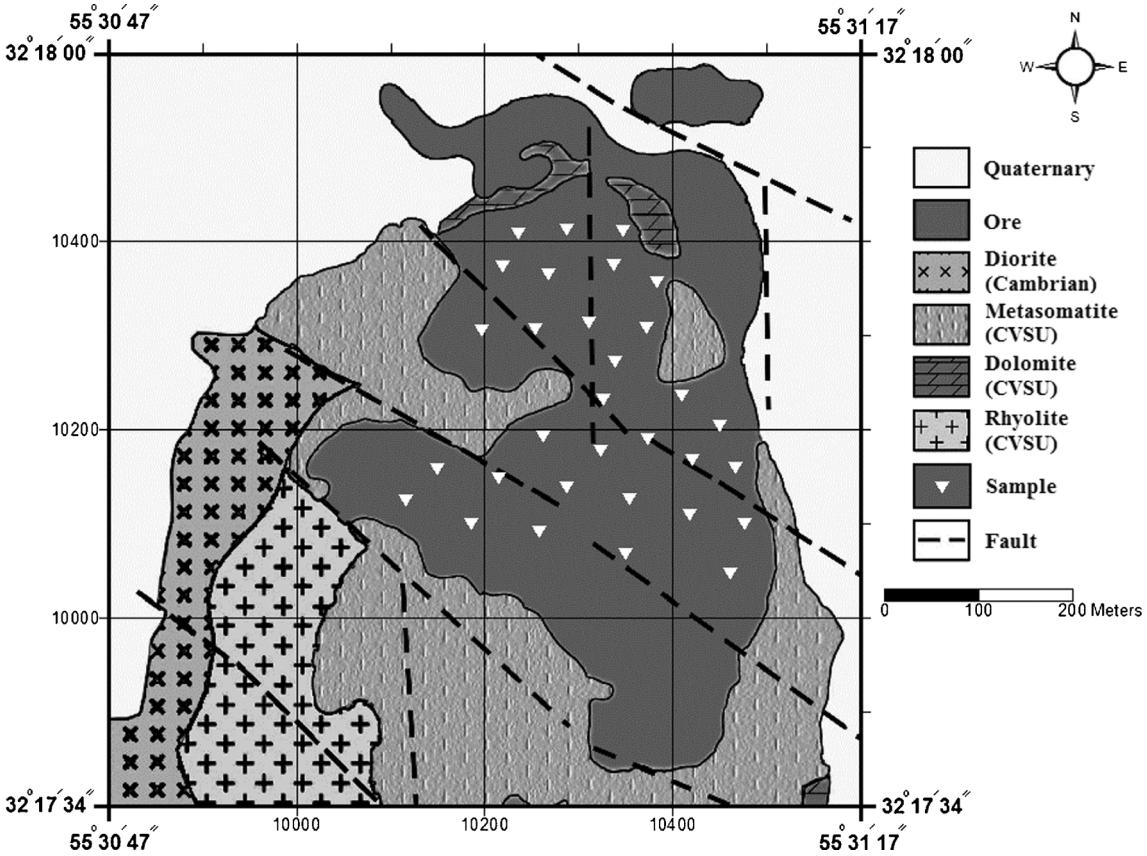

Fig. 3 Simplified geological map of the northern orebody of the Chador-Malu deposit displaying the distribution of ore samples (Modified from Jafarzadeh 1981; Moghtaderi et al. 2007; Torab 2008). The local coordinate system has been established by S.R.K. Consulting Co., and is used in the Chador-Malu mine. The entire map lies in the ring fracture zone shown in Fig. 2 (see the text)

The mineralogy of the Chador-Malu deposit is fairly simple compared to the Bafq district deposits further south (Sabet-Mobarhan-Talab and Alinia 2014). The ore minerals consist predominantly of magnetite and apatite (Fig. 6a). Subordinate amounts of pyrite may also be observed (Fig. 6b). Martitization is common in magnetite ores, particularly close to the contacts (Fig. 6c). Primary hematite, however, is less abundant in the ores (Fig. 6d). At least two generations of apatite can be identified in the Chador-Malu deposit: primary coarse-grained subhedral to euhedral (ApI) and secondary fine-grained anhedral (ApII) apatites (Fig. 6e, f). Although rare earth minerals such as allanite, bastnaesite, and monazite have a relatively important presence in some Bafq district deposits (e.g., Esfordi; Jami 2005), they were merely observed as inclusions (predominantly monazite; see Fig. 11) in the present study, and never as distinct rare earth mineralization. Likewise, the gangue minerals (predominantly actinolite) have a paragenetic importance in certain Bafq district deposits and can be present in the main stage of mineralization (e.g., Esfordi; Jami 2005); however, they were never observed in the Chador-Malu ores. Thus the Chador-Malu ores can simply be divided into two types: magnetite ± hematite

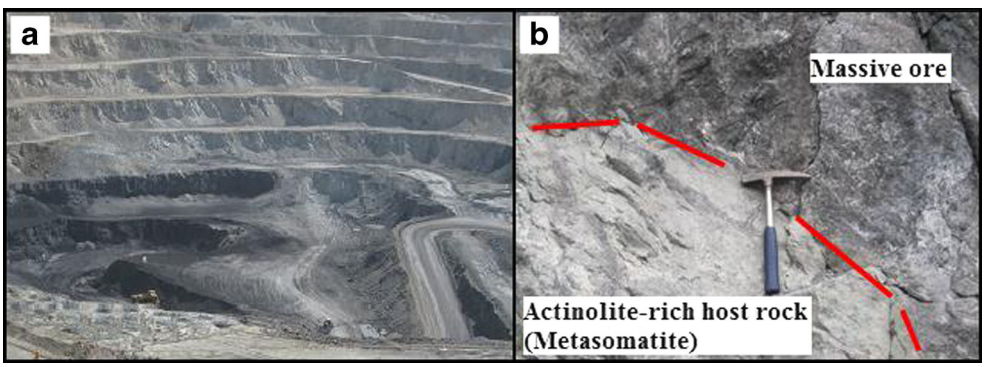

Fig. 4 The Chador-Malu iron oxide-apatite deposit. **a** A panorama showing part of the northern orebody (view to the east). **b** Sharp contact between the massive ore (dominant mineralization style) and the metasomatic host rock

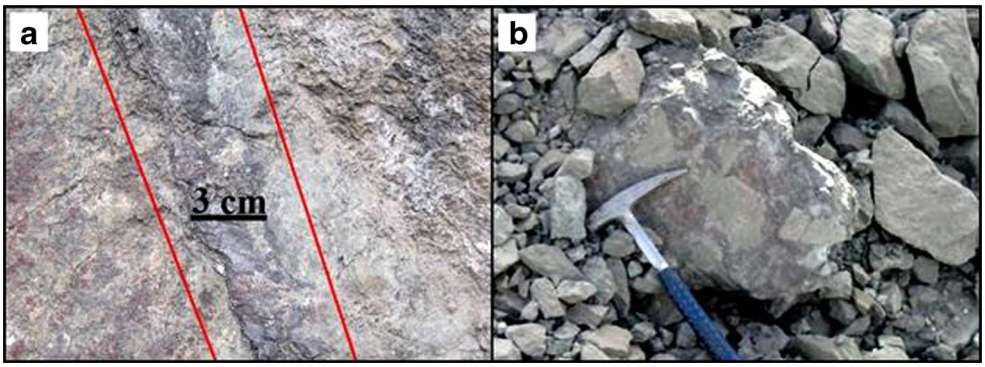

Fig. 5 Other styles of mineralization at Chador-Malu. **a** Small ore vein in the actinolite-rich host rock. **b** Angular brecciated fragments of the actinolite-rich country rocks cemented by iron oxides

ore (iron ore) and magnetite ± hematite + apatite ore (iron-apatite ore) (Fig. 7).

The actinolite-rich metasomatites comprise the main host rock to the northern orebody of the Chador-Malu deposit (Fig. 3). These rocks are the product of intense actinolitization that replaced most minerals in the pre-alteration protolith (Fig. 8a, b), giving the host rocks a distinctive green appearance (Figs. 4b and 5). Sodic (albitization) and potassic (K-feldsparization and sericitization) alterations can also be observed and are related to the earlier stages of regional metasomatism in the Bafq district (see also Daliran et al. 2007; Fig. 8c, d). Quartz represents the late stage of hydrothermal

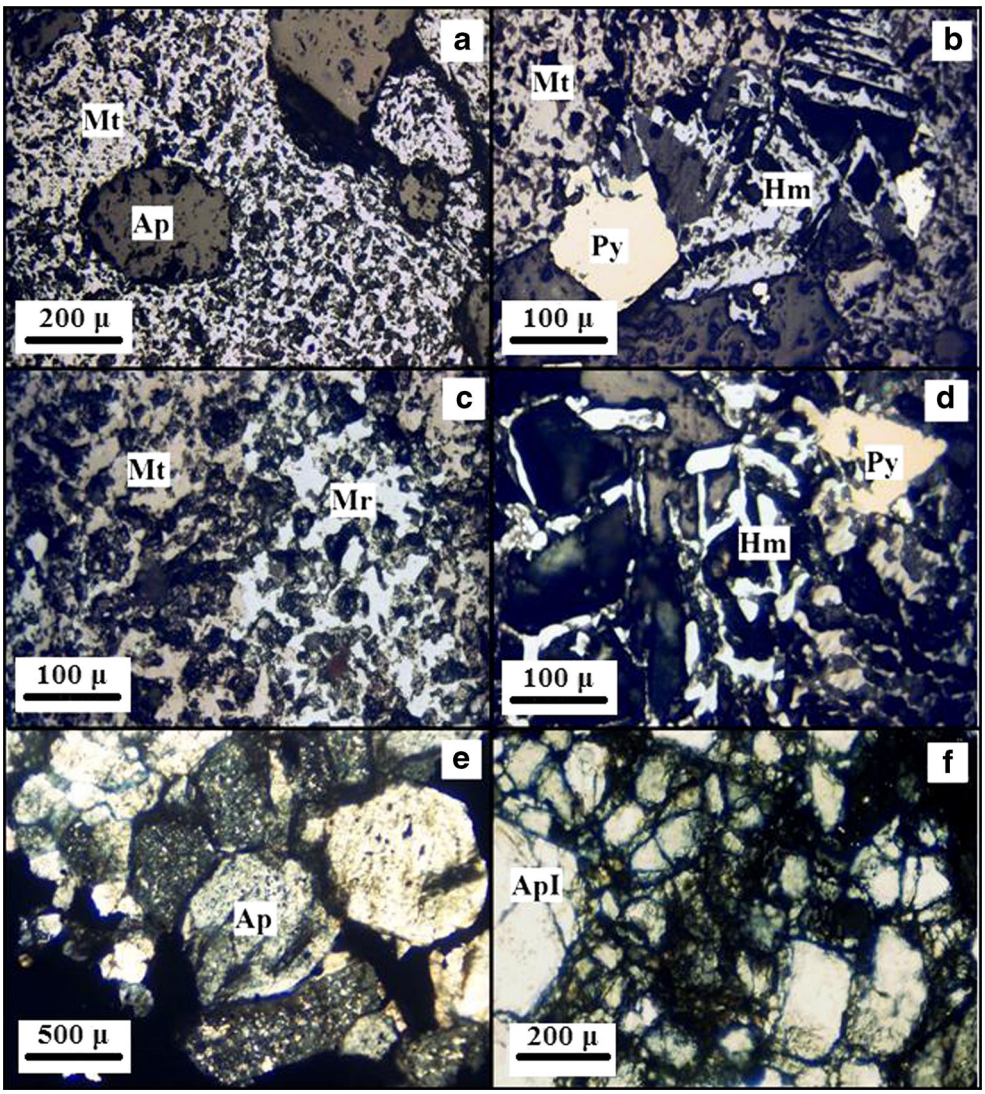

Fig. 6 Photomicrographs of the Chador-Malu ores. **a** Magnetite-apatite ore (reflected light). **b** Pentagonal pyrite in magnetite-hematite ore (reflected light). **c** Martitized magnetite ore. Note the preserved crystal form of magnetite in secondary hematite (reflected light). **d** Tabular texture in primary hematite (reflected light). **e** Iron-apatite ore with primary subhedral to euhedral apatite (ApI) in thin section (XPL). **f** Brecciated primary apatite (ApI) in a matrix of secondary fine-grained anhedral apatite (ApII) in thin section (XPL) (*Mt*: magnetite; *Hm*: hematite; *Mr*: martite; *Py*: pyrite; *Ap*: apatite)

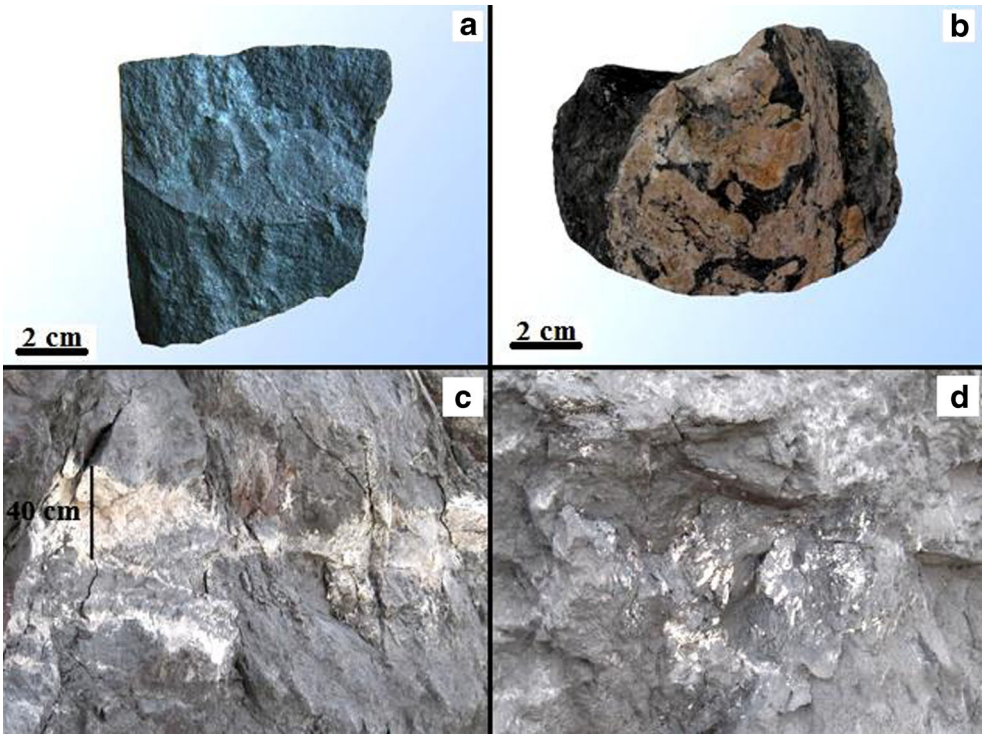

Fig. 7 The types of ore at Chador-Malu. **a**, **b** Hand specimens of rich magnetite (**a**; photograph from Torab 2008) and iron-apatite (**b**) ores. **c**, **d** Iron-apatite ore with aggregates of apatite (**c**) and with individual subhedral to euhedral apatite crystals (**d**) (the apatite crystals in the latter are up to 8 cm long)

alteration in the host rock (see also Daliran et al. 2007; Fig. 8e); however, at least part of the quartz (and other minerals) in the groundmass is relict magmatic (Fig. 8a, b, e). The host rocks may have locally undergone Fe-metasomatism which occurred subsequent to the multistage alteration of the host rock, resulting in the growth of magnetite grains on the alteration quartz (late stage) and other alteration minerals (Fig. 8).

Samples, analytical methods, and chemical compositions

Thirty-one ore samples, as well as eight magnetite and apatite mineral separates were collected from mined outcrops of the northern orebody of the Chador-Malu iron oxide-apatite deposit. The ore samples included iron ore (magnetite±hematite) and iron-apatite ore (magnetite±hematite+apatite). The magnetite samples were separated manually by means of magnet from plattner mortar-crushed rich magnetite ore specimens after removing contaminating fragments under a binocular microscope. The apatite samples were extracted from individual large subhedral to euhedral apatite crystals, as well as from patches of apatite in the ore (Fig. 7c, d). These apatite separates were prepared for analysis after it was confirmed by SEM that they were inclusion-free (4 from 17 examined samples in total). Additionally, the high-grade iron ore concentrate of two lines of the process plant were sampled to be included in iron oxide geochemistry. Five samples were also collected from the actinolite-rich metasomatic host rocks. A portion of the pulverized sample was accurately weighed into a PTFE tube, and a mixture of acids, including hydrofluoric acid, was added. The tube was then placed into a pressure vessel and sealed. The samples underwent digestion at high temperature and pressure (up to 200 °C and 20 Bar). After digestion, the samples were diluted to a predetermined volume, ready for analysis. The sample digest solutions were analyzed for major and trace element concentration by ICP-OES (PerkinElmer Optima 7300DV) and ICP-MS (PerkinElmer Nexion 300Q) at LabWest Minerals Analysis, Malaga, Western Australia. The resulting data were collated and assessed for performance of internal quality control results (blanks, duplicates, and certified reference materials) following LabWest's MMA-04 multielement analysis technique. The results are presented in Tables 1, 2, 3, and 4. Table 5 lists the locations of the ore samples based on the local coordinate system used in the Chador-Malu mine (see Fig. 3).

Results

Ferride distributions in iron oxides

Tables 1 and 3 present the ferride (Ti, V, Cr, Mn, Fe, and Ni) and some other trace metal (Al, Ca, and Co) contents of the iron oxides (iron ore samples as well as magnetite separates) from the Chador-Malu deposit.

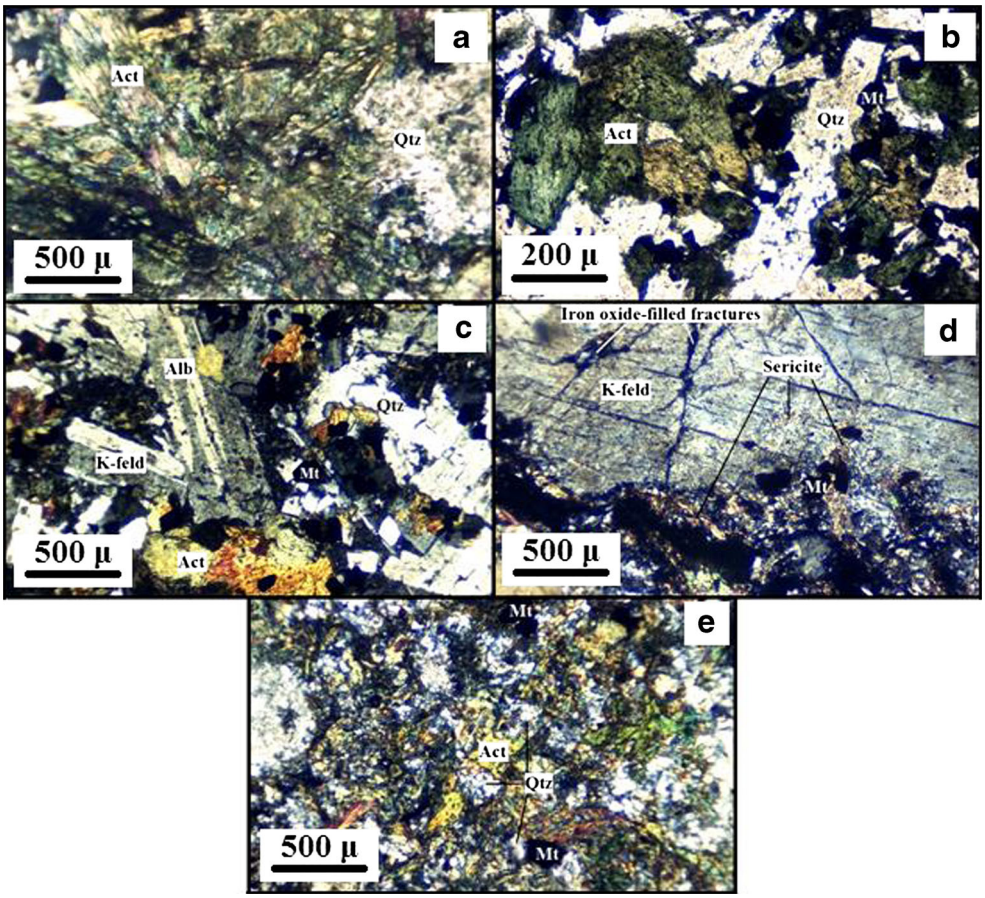

Fig. 8 Photomicrographs of the metasomatic host rock in thin section (XPL). **a**, **b** Actinolitization in the host metasomatite. Note the magnetite grains in **b. c** K-feldspar and albite in the host metasomatite representing the potassic and sodic alterations, respectively. Quartz represents the late stage of alteration. Note the magnetite growth on actinolite and quartz, and the actinolite crystal on albite, which demonstrate the order of crystallization. **d** Sericitization in the host metasomatite. Note the magnetite grains on sericitized K-feldspar. **e** Quartz growth on actinolite crystal occurred during the late stage of alteration (*Act*: actinolite; *Qtz*: quartz; *Mt*: magnetite; *K-feld*: potassium feldspar; *Alb*: albite)

The distribution of these metal concentrations (and associated ratios) in the samples is displayed on a compilation of variation diagrams (Fig. 9a–h). None of these diagrams attribute any sample to a BIF affinity. In spaces composed of various combinations of the ferride metals (diagrams constructed based on whole rock compositions; see Loberg and Horndahl 1983), the geochemical data indicate the Chador-Malu iron oxides to have compositions very similar to those of known Kiruna-type iron oxide-apatite deposits (Fig. 9a–e). Although the discriminant diagrams of Beaudoin et al. (2007), Beaudoin and Dupuis (2010), and Dupuis and Beaudoin (2011) (Fig. 9f–h) are constructed based on microanalytical data, the analytical data from our meticulously prepared magnetite separates from magnetite-rich specimens (see above; Fig. 7a) can yield reliable results on these diagrams. One magnetite sample falls in the reference field of the IOCG deposits in the discriminant diagram of Beaudoin and Dupuis (2010) (Fig. 9g), the one that also plots exactly on the boundary between the Kiruna-type and IOCG deposits in the discriminant diagram of Beaudoin et al. (2007) (Fig. 9f). However, when the average values of the data is plotted on the discriminant diagram of Beaudoin and Dupuis (2010) (as recommended by Dupuis and Beaudoin 2011), the data point (denoted by black cross) falls in the field of the Kiruna-type deposits (Fig. 9g). Likewise, the average value of the magnetite data on the discriminant diagram of Dupuis and Beaudoin (2011) signals a Kiruna-type affinity (Fig. 9h).

The Ti content of the iron oxide samples from the Chador-Malu deposit ranges from 294 to 6,270 ppm (Tables 1 and 3), which falls in the corresponding range for the Esfordi deposit (Bafq district) (200–15,000 ppm), with a considerable overlap between their samples (see Jami 2005 for Esfordi's data). Iron oxide samples of both deposits (Chador-Malu and Esfordi) are poor in Ti relative to the Mishdovan and Choghart deposits (Bafq district) which contain up to 2.5 wt% Ti (Daliran 1990) and 15 wt% Ti (Jami 2005), respectively, yet rich in Ti when compared to the classic Kiirunavaara deposit (northern Sweden) with samples containing up to 20 ppm Ti (Nyström and Henriquez 1994). The greater than an order of magnitude variation in the Ti content of the Chador-Malu iron oxide samples (294–6,270 ppm) may suggest the possibility of the contamination of some samples by discrete Ti mineral phases such as titanite; however, microscopic studies has shown that Ti minerals, and even their exsolution in magnetite, are very rare in the Chador-Malu iron oxide-apatite deposit (Sabet-Mobarhan-Talab and Alinia 2014; Sabet-Mobarhan-Talab 2014; Förster and Jafarzadeh 1994).

Table 1 Chemical composition of the iron ore samples (all concentrations in ppm except Fe)

Sample	DL (ppm)	IA01	IA04	IA06	IA11	IA14	IB01	IB03	IB05	IB06	IB09	IB10	IB12	IB18	IB25
Al	10	660	570	630	450	520	435	890	1,069	849	980	855	910	500	448
P	5	980	710	1,460	1,560	765	695	950	1,100	830	615	1,180	1,160	1,510	1,150
Ca	10	1,360	1,040	2,000	820	1,600	1,080	5,200	6,350	4,720	4,400	5,600	6,500	2,000	2,600
Ti	10	704	1,150	1,130	6,270	1,481	3,020	1,400	1,610	2,170	1,370	1,650	2,330	502	506
V	2	2,140	2,060	1,770	927	1,780	765	1,020	824	1,420	1,260	792	1,390	1,680	1,940
Cr	2	<2	21	25	27	41	26	15	10	16	13	28	20	16	36
Mn	2	320	224	147	152	124	138	163	194	335	120	306	218	223	213
Fe (%)	100	65.8	65.7	62.3	63.4	64.6	64.9	61.5	60.8	55.8	61.2	60	53	65.4	64.5
Co	0.2	46.8	51.5	43.1	33.8	58.8	31.3	30	28.1	31.1	40.8	31.4	34.8	26.9	43.2
Ni	2	139	134	125	182	237	202	176	169	291	181	265	100	133	136
La	0.05	139	105	109	97	69.5	70	92.6	75.2	48.6	113	70.3	117	135	132
Ce	0.05	388	272	292	255	185	186	276	233	138	284	218	331	386	358
Pr	0.05	45.7	34.9	35.1	32	22.8	24.6	39	33.9	20.4	38.5	32.8	40.9	46	41.3
Nd	0.02	180	123	117	115	79	91.6	151	134	79.6	146	130	166	180	155
Sm	0.02	26.5	19.4	16.6	18.8	11.8	16.3	29.8	28.3	17.2	29.2	27	31.5	27.2	23.3
Eu	0.02	2.31	1.97	1.43	2.63	1.05	1.53	2.66	2.77	1.72	3.44	3.02	3.27	2.1	1.95
Gd	0.05	22.3	16.8	16	16.2	11	12.1	23.5	21.9	12.5	22.1	18.9	24.5	22.6	21
Tb	0.02	2.78	2.19	1.99	2.3	1.48	1.73	5.16	5.54	3.19	3.75	4.25	4.51	3	2.62
Dy	0.02	13.3	10.2	9.74	11.7	7.48	8.83	30.1	33.9	19.8	19	24.4	24.3	14.5	12
Ho	0.02	2.27	1.74	1.72	2.18	1.37	1.56	6.27	7.35	4.09	3.42	4.97	4.45	2.53	2.07
Er	0.05	5.75	4.33	4.31	5.72	3.61	4.33	16.8	20.2	11	9.03	13.6	11.2	6.39	5.03
Tm	0.05	0.76	0.63	0.6	0.82	0.5	0.66	2.43	3	1.66	1.39	2.05	1.59	0.85	0.66
Yb	0.05	3.92	3.11	3.2	4.34	2.55	3.87	12.9	16.1	8.79	7.76	11.6	8.58	4.21	3.36
Lu	0.02	0.61	0.46	0.46	0.59	0.35	0.58	1.77	2.29	1.17	1.1	1.68	1.11	0.57	0.45
Eu/Eu^*		0.289	0.331	0.266	0.458	0.280	0.331	0.305	0.338	0.356	0.411	0.406	0.357	0.257	0.268
$(La/Yb)_N$		24.55	23.38	23.58	15.47	18.87	12.52	4.97	3.23	3.83	10.08	4.20	9.44	22.20	27.20

$Eu/Eu^* = Eu_{cn}/(Sm_{cn} \times Gd_{cn})^{1/2}$

Table 2 P and REE composition of the iron-apatite ore samples (all concentrations in ppm except P)

	P (%)	La	Ce	Pr	Nd	Sm	Eu	Gd	Tb	Dy	Ho	Er	Tm	Yb	Lu	∑REE	Eu/Eu*	$(La/Yb)_N$
DL (ppm)	5	0.05	0.05	0.05	0.02	0.02	0.02	0.05	0.02	0.02	0.02	0.05	0.05	0.05	0.02			
Sample																		
IA102	2.30	174	476	54.8	213	32	2.62	29	4.03	20.4	3.77	9.5	1.24	6.21	0.86	1,027.43	0.261	19.40
IA103	1.85	259	635	67.9	250	35.2	2.89	36.9	3.93	17.9	3.06	7.59	1	4.9	0.69	1,325.96	0.243	36.60
IA105	1.70	203	554	63.2	243	35.8	2.97	31.6	4.11	19.5	3.52	8.36	1.1	5.83	0.82	1,176.81	0.268	24.11
IA107	1.95	209	556	62.5	236	35	2.83	32.5	4.23	21.3	3.73	9.28	1.21	6.08	0.8	1,180.46	0.255	23.80
IA108	1.73	190	506	56.2	211	31.5	2.49	29.4	3.8	18.7	3.37	8.66	1.13	5.67	0.76	1,068.68	0.248	23.20
IA112	1.72	202	561	63.9	245	36.8	2.98	33.4	4.47	22.2	4.02	10.2	1.34	6.82	0.93	1,195.06	0.258	20.51
IA113	1.51	204	534	59.5	222	31.5	2.8	30.5	3.69	17.9	3.1	7.75	1.05	5.37	0.72	1,123.88	0.274	26.30
IA215	1.69	242	655	75.4	290	42	3.19	38.1	4.89	23.6	4.23	10.8	1.42	7.15	0.97	1,398.75	0.242	23.43
IA216	2.16	271	726	82.3	313	46	3.58	43.1	5.48	26.8	4.83	12.2	1.61	8.48	1.05	1,545.43	0.244	22.13
IA217	1.56	190	502	57.2	216	32.4	2.57	30	3.91	19.7	3.54	9.06	1.2	5.99	0.83	1,074.40	0.250	21.96
IA220	2.80	431	1,120	123	425	66	5	66.4	8.04	39.2	7.16	18.1	2.34	11.5	1.54	2,324.28	0.229	25.95
IA221	2.03	248	662	74	277	40.4	3.05	38.7	4.98	24.6	4.54	11.5	1.53	7.82	1.07	1,399.19	0.234	21.96
IA222	2.21	198	524	59	219	31.9	2.46	30.2	3.72	17.9	3.25	8.16	1.1	5.42	0.73	1,104.84	0.241	25.29
IA223	2.25	368	940	104	354	54.3	4.3	52.6	5.96	27.9	4.75	11.7	1.55	7.49	1	1,937.55	0.244	34.02
IA224	1.96	303	783	86	296	47.1	3.82	45.7	5.2	24.2	4.2	10.2	1.39	6.82	0.95	1,617.58	0.250	30.76
IA303	4.11	572	1,500	166	568	91.6	9.17	93.4	10.9	52.3	9.22	22.7	3.01	16	2.02	3,116.32	0.301	24.75
IA325	2.46	405	1,040	113	392	62.7	4.88	60.4	7.55	36.5	6.53	16.4	2.14	10.7	1.47	2,159.27	0.241	26.21

$Eu / Eu^{*} = Eu_{cn} / (Sm_{cn} \times Gd_{cn})^{1/2}$

Table 3 Chemical composition of the mineral samples (prepared mineral separates) and the high-grade iron ore concentrate (all concentrations in ppm unless indicated otherwise)

Sample	DL (ppm)	Ap1	Ap2	Ap3	Ap4	Mt1	Mt2	Mt3	Mt4	Conc1	Conc2
Al	10					243	170	280	144	1,470	1,500
P	5	20.10 %	20.50 %	19.00 %	20.90 %	420	512	540	340	1,640	1,730
Ca	10					320	420	250	540	3,480	3,970
Ti	10					3,260	3,740	3,130	294	867	658
V	2					1,830	1,910	1,910	1,680	1,850	1,760
Cr	2					46	35	41	71	16	16
Mn	2	83	87	74	79	136	125	143	109	135	146
Fe (%)	100					71.3	69.5	70.2	68.7	64.6	62.1
Co	0.2					36.3	36.6	34.9	14.1	30.3	30.4
Ni	2					212	246	326	143	145	141
Sr	0.1	240	336	246	496						
Y	0.05	752	741	612	1,310						
La	0.05	2,416	2,083	1,771	3,020	44	30	19	39.2	37.4	35.3
Ce	0.05	4,354	5,287	4,229	6,220	98.8	69.3	51.5	104	87.5	81.3
Pr	0.05	624	708	495	833	10.22	8.89	6.74	11.84	10.6	10.2
Nd	0.02	2,248	2,107	1,369	2,810	33.72	34.42	24.3	45.2	35.6	33.9
Sm	0.02	284	304	182	406	4	5	3.5	6.66	5.03	4.85
Eu	0.02	26.25	28	13.5	35	0.32	0.41	0.23	0.49	0.44	0.44
Gd	0.05	260	223	179	414	3.4	4.04	3	5.6	4.85	5.29
Tb	0.02	37.45	28.6	23.85	46.08	0.47	0.49	0.42	0.71	0.59	0.6
Dy	0.02	160	133	117	220	2.52	2.34	2.09	3.56	2.91	2.7
Ho	0.02	27.12	24.48	20.07	37.71	0.44	0.43	0.35	0.63	0.51	0.43
Er	0.05	71.6	59.58	47.7	104	1.12	0.96	0.93	1.59	1.34	1.2
Tm	0.05	8.4	6.93	5.34	12.33	0.18	0.13	0.11	0.2	0.2	0.17
Yb	0.05	40	33.12	25.83	66.24	0.78	0.8	0.69	1.04	1.04	0.96
Lu	0.02	5.6	4.17	3.3	8.8	0.18	0.1	0.08	0.13	0.14	0.13
∑REE		10,562.4	11,029.9	8,481.6	14,233.2	200.1	157.3	112.9	220.8	188.1	177.5
Eu/Eu^*		0.293	0.327	0.227	0.259	0.263	0.277	0.216	0.244	0.271	0.264
$(La/Yb)_N$		41.82	43.54	47.47	31.57	39.06	25.96	19.07	26.10	24.90	25.46

Apatite samples: Ap1, Ap2, Ap3, Ap4; Magnetite samples: Mt1, Mt2, Mt3, Mt4; High-grade iron ore concentrate: Conc1, Conc2

$Eu / Eu^* = Eu_{cn} / (Sm_{cn} \times Gd_{cn})^{1/2}$

Apatite Y-Sr compositions and apatite-monazite relationship

Y-Sr composition of apatite samples (mineral separates) from the Chador-Malu deposit indicates a Kiruna-type iron ore and mafic rock genetic association (Fig. 10).

Several apatite samples were examined by SEM in order to select inclusion-free apatites for chemical analysis (see above). Monazite inclusions were observed in most apatite samples. Figure 11 shows an example of monazite-bearing apatite. Such monazite inclusions (Fig. 11) may nucleate through REE redistribution in apatite through fluid-mineral interaction (e.g., Harlov and Förster 2003; Harlov et al. 2005), and are typical of the classic Swedish Kiruna-type deposits (e.g., Parak 1975; Harlov et al. 2002). Apatite REE leaching and monazite formation in Kiirunavaara deposit was ongoing through infiltration of high-temperature brines (700–800 °C), which were originated from the source magma subsequent to the magmatic emplacement of a proposed Fe-P melt (Harlov et al. 2002). Monazite inclusions have also been observed in the apatites from other Bafq district deposits (e.g., Torab and Lehmann 2007; Stosch et al. 2011; Bonyadi et al. 2011).

REE concentrations and chondrite-normalized patterns

REE compositions of the samples from the Chador-Malu deposit are listed in Tables 1, 2, 3, and 4. The REE content of the mineral separates of apatite ranges from 0.85 to 1.42 wt%, but is above 1 wt% in three of the them (Table 3). The total REE content of the magnetites (mineral separates) and iron ore

Table 4 REE, P, Na, K, and Ca composition of the host rocks (all concentrations in ppm unless indicated otherwise)

Sample	DL (ppm)	CHR1a	CHR1b	CHR2	OCHR1	OCHR2
Description		Act-rich	Act-rich	Act-rich	Act-rich	Act-rich
Longitude		10,509.3	10,509.3	10,503.5	10,511.2	10,516.1
Latitude		10,040.7	10,040.7	10,031.9	10,032.9	10,030.0
Na (%)	10	0.77	1.12	0.28	1.20	1.78
K (%)	10	0.32	1.70	0.72	2.50	1.10
Ca (%)	10	4.70	4.15	4.30	4.90	4.60
P	5	470	320	240	430	640
La	0.05	155	105	67.3	38.1	68.0
Ce	0.05	439	294	191	123	219
Pr	0.05	57.2	42.5	30.2	19.2	33.3
Nd	0.02	228	160	121	70.4	100
Sm	0.02	41.1	29.4	20.9	13.2	18.1
Eu	0.02	4.00	3.90	2.12	1.12	1.60
Gd	0.05	34.1	22.9	16.8	10.9	15.0
Tb	0.02	5.88	3.70	4.10	1.32	1.80
Dy	0.02	33.1	19.4	24.5	6.84	8.80
Ho	0.02	6.30	3.53	5.01	1.23	1.50
Er	0.05	18.0	10.1	15.1	3.25	3.50
Tm	0.05	2.44	1.46	2.19	0.42	0.50
Yb	0.05	15.2	9.50	13.8	2.10	3.20
Lu	0.02	2.26	1.48	2.03	0.32	0.41
∑REE		1,041.6	706.9	516.1	291.4	474.7
∑LREE		920.3	630.9	430.4	263.9	438.4
$(La/Lu)_N$		7.10	7.35	3.43	12.33	17.17
$(La/Sm)_N$		2.36	2.24	2.02	1.81	2.35
$(Gd/Lu)_N$		1.86	1.91	1.02	4.21	4.52
Eu/Eu^*		0.324	0.456	0.344	0.284	0.295

CHR1a and CHR1b are collected with approx. 1 m spacing at the same sampling location

concentrate is below 220 ppm, and can be as low as 112 ppm (Table 3). This value ranges from 0.1 to 0.23 wt% for the iron-apatite ore samples, but is commonly lower than 0.15 wt% (Table 2).

The chondrite-normalized REE patterns of the Chador-Malu apatite (mineral separates), magnetite (mineral separates), iron ore, iron-apatite ore, and high-grade iron ore concentrate, as well as the Chador-Malu and the Zarigan granites are represented in Fig. 12a–d. The REE distribution in the Chador-Malu magnetite is similar to those of the apatite (Fig. 12c). The REE patterns of the iron-apatite ore samples also resemble those of the apatites (Fig. 12a). However, the REE patterns of the iron ore samples show two different trends, particularly in the heavy rare earth element (HREE) portion with one branch of elevated curves (Fig. 12b).

We noticed that the iron ore samples with elevated HREE patterns (Fig. 12b) have higher Ca contents (>0.44 %) than other iron ore samples (<0.26 %). The actinolite-rich host rock of the Chador-Malu deposit has locally undergone intense Fe-metasomatism (Sabet-Mobarhan-Talab 2014). It is therefore very likely to have ore samples contaminated with minor amounts of the actinolite-rich host rock, particularly when collecting samples near the contacts. This might account for the relatively high Ca contents of some of the iron ore samples (Table 1).

The REE patterns of the actinolite-rich host rock samples are shown in Fig. 13. Three host rock samples were collected adjacent to the contacts (CHR1a, CHR1b, and CHR2; see Table 4 for coordinates). These samples show elevated HREE patterns. However, two host rock samples were collected at some distance (up to 20 m) from the contacts (OCHR1 and OCHR2; Table 4). The latter have REE patterns similar to most other minerals and ores (Figs. 12a–c and 13). While in magmatic liquids, middle rare earth elements (MREE) are more compatible in amphiboles than HREE (e.g., Rollinson 1993), and the systematics of REE partitioning between fluid and mineral phases in relevant geological conditions to this study are not yet well-established, it can be postulated that the

Table 5 Location of the ore samples based on the local coordinate system used in the Chador-Malu mine

Sample	Description	Longitude	Latitude
IA01	Iron ore	10,235.5	10,410.1
IA04	Iron ore	10,218.7	10,374.7
IA06	Iron ore	10,335.5	10,376.5
IA11	Iron ore	10,311.2	10,316.8
IA14	Iron ore	10,338.3	10,273.7
IB01	Iron ore	10,185.1	10,101.9
IB03	Iron ore	10,214.9	10,151.5
IB05	Iron ore	10,262.7	10,196.3
IB06	Iron ore	10,326.1	10,234.5
IB09	Iron ore	10,410.3	10,237.3
IB10	Iron ore	10,450.4	10,206.6
IB12	Iron ore	10,466.3	10,162.7
IB18	Iron ore	10,258.0	10,094.4
IB25	Iron ore	10,354.1	10,128.9
IA102	Iron-apatite ore	10,287.9	10,414.8
IA103	Iron-apatite ore	10,346.7	10,413.9
IA105	Iron-apatite ore	10,268.1	10,367.2
IA107	Iron-apatite ore	10,382.1	10,359.7
IA108	Iron-apatite ore	10,370.9	10,310.3
IA112	Iron-apatite ore	10,253.2	10,309.3
IA113	Iron-apatite ore	10,196.3	10,306.5
IA215	Iron-apatite ore	10,476.5	10,102.8
IA216	Iron-apatite ore	10,460.7	1,0049.6
IA217	Iron-apatite ore	10,349.5	10,071.1
IA220	Iron-apatite ore	10,286.9	10,141.2
IA221	Iron-apatite ore	10,323.3	10,179.5
IA222	Iron-apatite ore	10,372.8	10,192.5
IA223	Iron-apatite ore	10,420.5	10,170.1
IA224	Iron-apatite ore	10,417.7	10,112.1
IA303	Iron-apatite ore	10,116.0	10,126.1
IA325	Iron-apatite ore	10,149.6	1,0161.7

interaction of a fluid with a high HREE/LREE fractionation (see below) with the actinolite-rich host rocks could produce the HREE-elevated chondrite-normalized patterns of the host rock samples (Fig. 13). Thus the hydrothermal mobilization of the apatite-hosted REE during overprinting, apatite leaching and monazite formation (see above; Fig. 11) could be proposed. This process would involve the release of the REE, particularly the HREE, from apatite to produce the fluid with high HREE/LREE fractionation proposed above. The HREE would more readily enter the fluid phase since they would not be significantly partitioned into the crystallizing monazite inclusions, and are more susceptible to complexing (Humphris 1989) due to their relatively higher field strength (Rollinson 1993). The uptake of the HREE by abundant actinolite in the host rocks would be important. This hypothesis, however, needs to be verified by further investigation. This translocation of the REE was most probably restricted to the adjacent host rocks which is suggested by the REE patterns of the host rocks close to (CHR1a, CHR1b, and CHR2) and away from (OCHR1 and OCHR2) the contacts with the ore (Fig. 13). This observation is consistent with the mobility of up to several centimeters for the REE during apatite leaching and monazite formation in the Se-Chahun iron oxide-apatite deposit proposed by Bonyadi et al. (2011). It is also clear that the elevated HREE patterns of the iron ore samples mentioned above (Fig. 12b) are due to the contamination with small amounts of the adjacent actinolite-rich host rocks.

The degree of LREE/HREE fractionation, represented by $(La/Yb)_N$ ratio, ranges from 31.57 to 47.47 for the apatites, from 19.07 to 39.06 for the magnetites, from 24.90 to 25.46 for the high-grade iron ore concentrate, and from 19.40 to 36.60 for the iron-apatite ore samples and indicates light rare earth element (LREE) enrichment relative to HREE; but it ranges from 3.23 to 27.20 for the iron ore samples, which display two distinct HREE trends. The extent of LREE/HREE fractionation can also be represented by $(La/Lu)_N$ ratio, which in the case of actinolite-rich host rocks, ranges from 3.43 to 7.35 for the samples adjacent to the contacts (CHR1a, CHR1b, and CHR2), and for the other two samples away from the contacts (OCHR1 and OCHR2) is 12.33 and 17.17.

Overall, except for the iron ore samples with raised HREE patterns, almost all ore and mineral samples display REE patterns that follow the same path, particularly in their MREE and HREE portions. All these REE patterns can be described as similar, regarding their steep slope with relatively high LREE/HREE fractionation and the negative Eu anomaly (Fig. 12a–c).

The chondrite-normalized REE pattern of the Chador-Malu granite is significantly different from the iron oxide-apatite deposit, mainly in terms of LREE/HREE fractionation and Eu anomaly (Fig. 12d). Interestingly, the REE pattern of the Zarigan granite, which is located further south in the Bafq district, and is associated with iron oxide-apatite mineralization (Fig. 2), is very similar to the Chador-Malu granite (Fig. 12d).

Discussion

Geochemistry of iron oxides

The geochemistry of iron oxides can indicate the mineral deposit type to which they belong (e.g., Loberg and Horndahl 1983; Beaudoin and Dupuis 2010; Dupuis and Beaudoin 2011; Nadoll et al. 2012). While some major Bafq district iron oxide-apatite deposits have been related to the Rapitan-type banded iron-phosphorus formations (e.g., Aftabi et al. 2009;

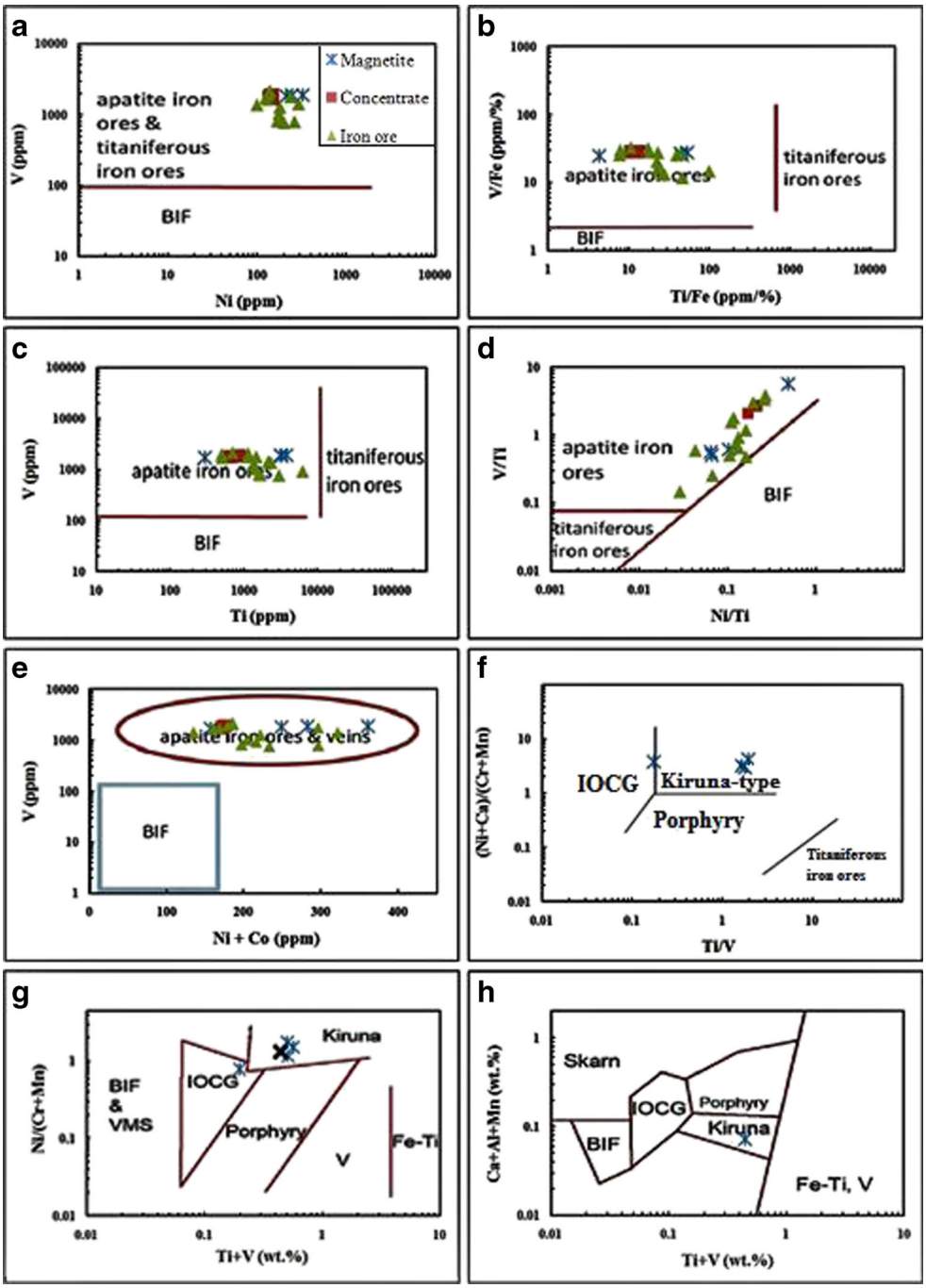

Fig. 9 Trace element diagrams of iron oxides. The legend included in "**a**" describes the symbols used in the entire figure. **a**–**e** Iron oxide data in various ferride spaces indicating deposit types. All diagrams after Loberg and Horndahl (1983). **f** Magnetite data points showing a Kiruna-type affinity. Note the one data point exactly on the boundary between the Kiruna-type and IOCG deposits. Diagram after Beaudoin et al. (2007). **g** Magnetite data points showing deposit types. Average data point is denoted by black cross. Note the one magnetite data point in the IOCG field. See the text for interpretation. Diagram after Beaudoin and Dupuis (2010). **h** Average data point of magnetite indicating a Kiruna-type affinity. Diagram after Dupuis and Beaudoin (2011)

Mohseni and Aftabi 2012), the ferride and trace element geochemistry of the iron oxide samples (iron ores and magnetite separates) from Chador-Malu does not suggest any BIF affinity (Fig. 9). Instead, the whole rock composition of the Chador-Malu iron ores, as well as the composition of the prepared magnetite separates, are similar to the whole rock composition of the Kiruna-type iron ores, including the Swedish ones (see Loberg and Horndahl 1983; Fig. 9a–e), for which direct magmatic genetic models have been proposed by several authors (e.g., Philpotts 1967, 1982; Frietsch 1978, 1984; Nyström and Henriquez 1994; Naslund et al. 2000; Jonsson et al. 2013); however, such models are highly disputed and no longer widely accepted. The composition of the magnetite separates (and/or their average composition) is similar to the mineral composition of the Kiruna-type magnetites (Fig. 9f–h), with one exception which shows an IOCG attribute on the diagrams in Fig. 9f, g. The similar ferride and trace element geochemistry of the iron oxides from Chador-Malu and other Kiruna-type deposits may indicate similar ore-forming processes in their genesis. Additionally, the

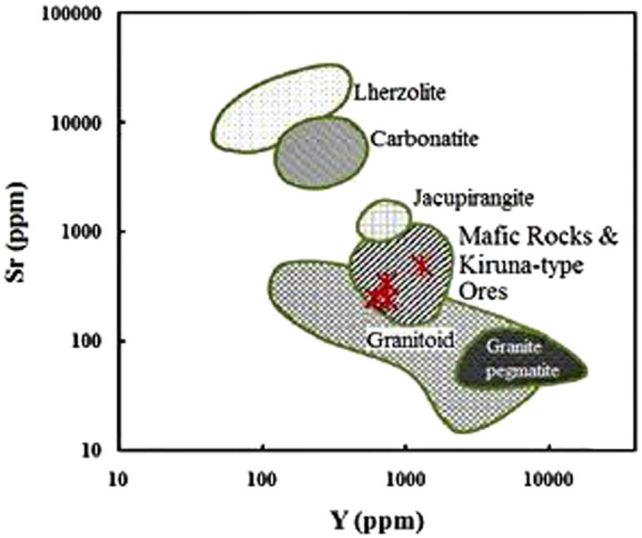

Fig. 10 Y-Sr composition of the Chador-Malu apatites. Diagram after Belousova et al. (2002)

distribution of Ti concentration in the iron oxide samples from the Chador-Malu and Esfordi deposits is similar (see above). Jami (2005) proposed that the mineralizing fluids at Esfordi were in equilibrium with immiscible Fe-P melts. Similar fluids may have been involved in the formation of the Chador-Malu deposit.

Moreover, the position of the magnetite data points on the diagrams in Fig. 9 can be indicative of some comparable features the geochemistry of the Kiruna-type and Cu-Au-bearing IOCG deposits may have, both of which having been grouped together as the end-members of the IOCG clan according to the classification by Hitzman et al. (1992) (see also Groves et al. 2010).

Texture and composition of apatites

The Y-Sr composition of the Chador-Malu apatites (Fig. 10) supports the finding of Torab and Lehmann (2007) that the Bafq apatites are chemically very similar to those of other Kiruna-type deposits (see also Bonyadi et al. 2011). However, these results are not consistent with the previous discussions suggesting a carbonatitic affinity for apatites of the Bafq district deposits (e.g., Daliran 2002; Darvishzadeh 1983; Darvishzadeh and Aletaha-Kohbanani 1996). Carbonatitic apatites are characterized by high Sr (commonly more than 2, 500 ppm) and relatively low Y contents (commonly less than 400 ppm) (Belousova et al. 2002), which is not the case in the Chador-Malu deposit (Table 3; Fig. 10).

The apatite REE leaching and monazite formation in the Chador-Malu deposit (Fig. 11) can be associated with a high-temperature overprinting event similar to the classic Kiirunavaara deposit (Harlov et al. 2002). The formation of second generation fine-grained anhedral apatite (ApII), which is associated with primary coarse-grained subhedral to euhedral apatite (Fig. 6f), can also be related to the same overprinting event, and is consistent with the restricted mobility of P (millimeters to centimeters) in the high-temperature brines responsible for apatite REE leaching and associated monazite formation (see Bonyadi et al. 2011). These textural

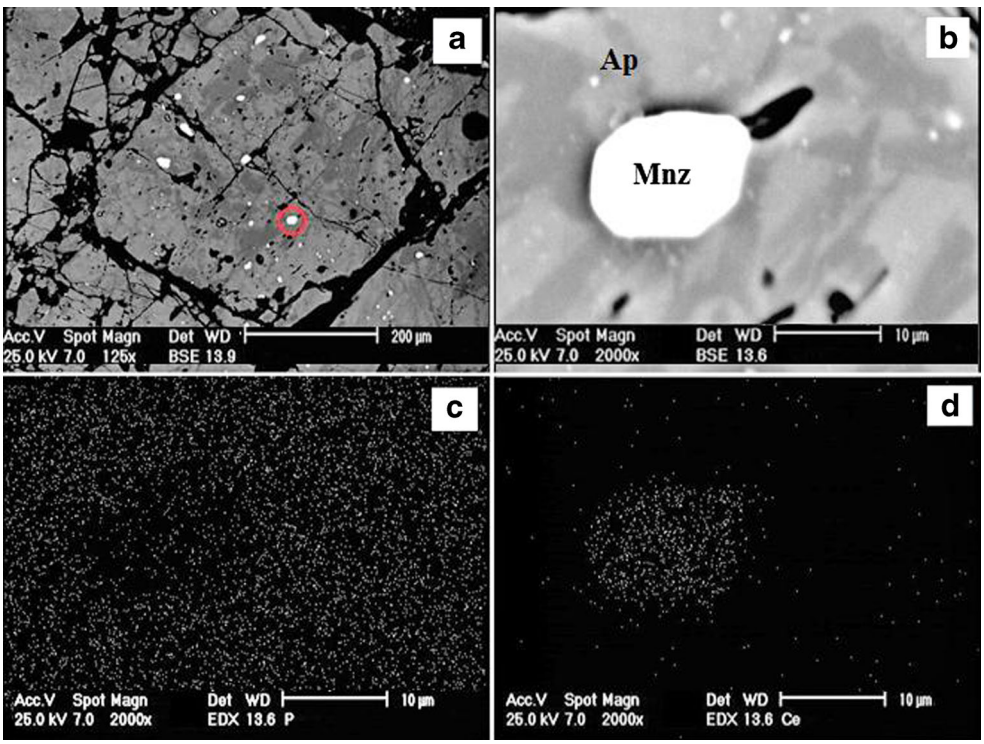

Fig. 11 Backscattered Electron (BSE) images and elemental maps of the Chador-Malu apatite. **a** BSE-bright and BSE-dark patterns and monazite inclusions in brecciated apatite indicating REE redistribution during fluid-mineral interaction. **b** Magnified BSE image of the monazite inclusion circled in "a". **c** and **d** Elemental maps of the inclusion in "b" verifying that the Ce-rich phosphate phase is actually monazite (*Ap*: apatite; *Mnz*: monazite)

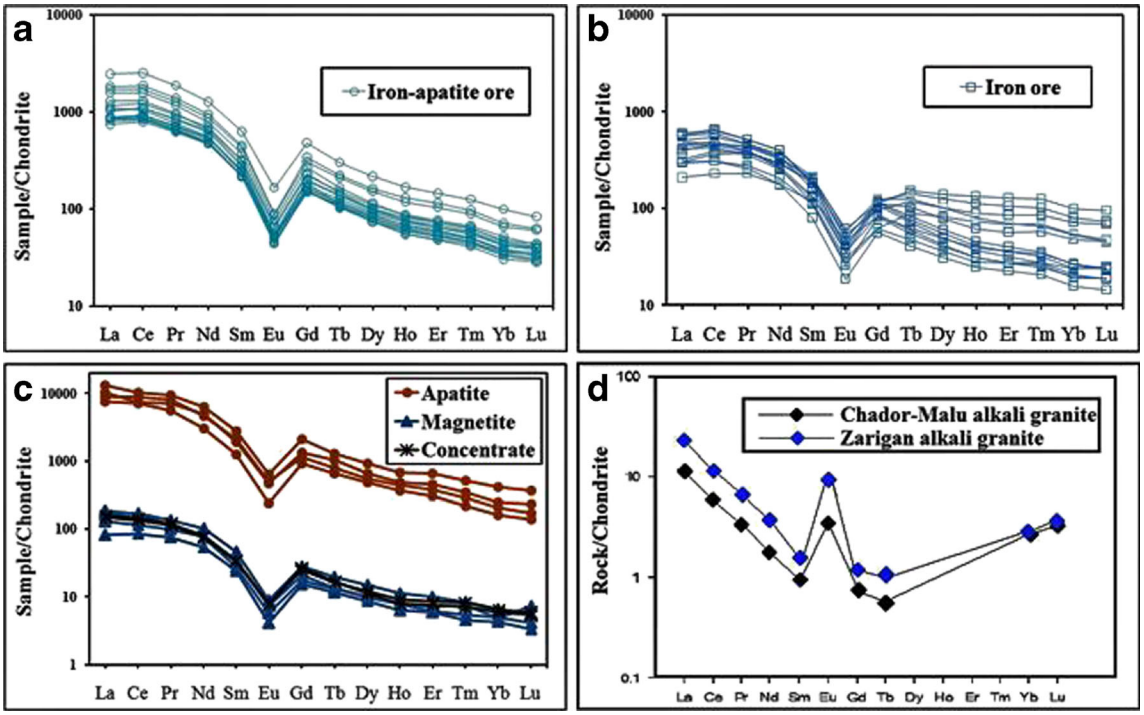

Fig. 12 Chondrite-normalized REE patterns of the Chador-Malu deposit and granite. **a** REE patterns of the iron-apatite ore samples. **b** REE patterns of the iron ore samples. Note that HREE patterns branch into two trends. See the text for interpretation. **c** Similar apatite, magnetite, and iron ore concentrate REE patterns. **d** REE pattern of the Chador-Malu granite. Note the similar REE pattern of the Zarigan granite. See the text for interpretation. Analytical data of the granites from Ramezani and Tucker (2003). Chondrite values from Anders and Grevesse (1989)

observations argue for metasomatism and highlight the importance of high-temperature hydrothermal fluids at Chador-Malu. A magmatic source for similar brines is proposed at Kiruna (Harlov et al. 2002, 2005; Harlov and Förster 2003).

REE patterns and their significance

Similar magnetite and apatite REE patterns have widely been interpreted as an indicator of their common origin (see, e.g., Frietsch and Perdahl 1995; Nabatian et al. 2012; Mokhtari et al. 2013, among others). The REE patterns of the magnetite and apatite samples from Chador-Malu are very similar in terms of their LREE/HREE fractionation and negative Eu anomalies (Fig. 12c; Table 3). This can suggest a common origin for these minerals. However, the magnetites may have inherited their REE patterns (Fig. 12c) from micro inclusions of apatite and/or fluid-mineral interaction during the hydrothermally overprinting events discussed above.

Almost all mineral and ore samples (except the HREE-elevated iron ores) from Chador-Malu have REE patterns similar to the Kiruna-type deposits from northern Sweden (see,

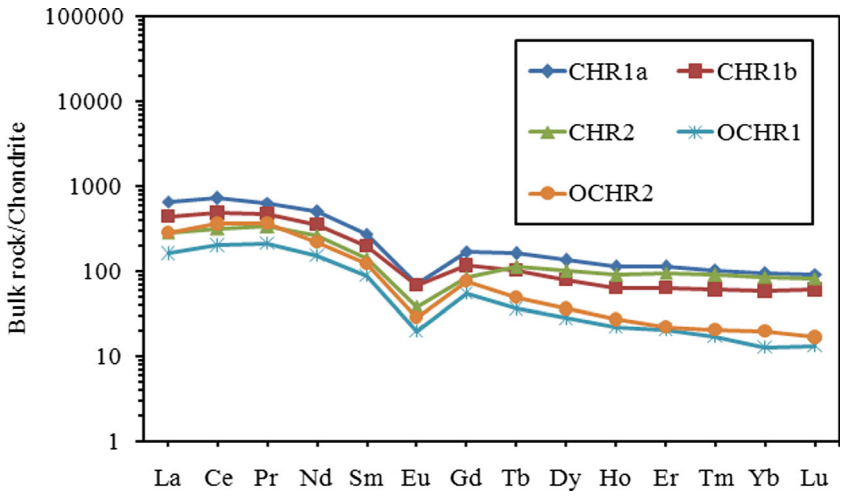

Fig. 13 Chondrite-normalized REE patterns of the actinolite-rich metasomatic host rocks. Chondrite values from Anders and Grevesse (1989)

e.g., Frietsch and Perdahl 1995; Harlov et al. 2002). There are also other Bafq district iron oxide-apatite deposits which share the same typical REE patterns (see, e.g., Jami 2005; Torab 2008; Bonyadi et al. 2011, among many others). This demonstrates that the regional processes involved in the metallogeny of the Bafq district can be similar to the Kiruna district.

Genetic discussion

A potential source for Fe and P

There is consensus in the literature that the close spatial and temporal association of iron oxide-apatite deposits with igneous rocks is consistent with magma as a direct or indirect source of Fe and P (see the review above). Supporting a magmatic origin, Förster and Jafarzadeh (1994) pointed out melt flow and quench textures in the Bafq district. Such features have also been reported for the Kiirunavaara and El Laco iron oxide-apatite deposits by Harlov et al. (2002) and Naslund et al. (2002), who considered the mineralization to be the product of direct crystallization from immiscible iron oxide melts. Field evidence for an iron oxide-dominated magma (e.g., magnetite-bearing pyroclastic rocks and lava flows) have been reported from Sweden, Chile, and Iran (e.g., Frietsch 1978; Nyström and Henriquez 1994; Förster and Jafarzadeh 1994). Iron ± titanium ± phosphorus melts have also been produced experimentally by immiscible separation from silica-rich liquids (e.g., Philpotts 1967; Naslund 1983). Such immiscible iron oxide melts, into which phosphorus is strongly partitioned (Clark and Kontak 2004), can be generated in various thermodynamic and physicochemical conditions (Hurai et al. 1998), as a late-stage differentiate of the magmatism (e.g., Frietsch and Perdahl 1995). In the Bafq district terms, differentiating alkaline mafic magmas may have generated immiscible Fe-P melts, as suggested by Förster and Jafarzadeh (1994). From a regional point of view, the major granitic intrusions of the Bafq district (i.e., Chador-Malu and Zarigan granites; Fig. 2) could be assumed to be the alkaline silicic residue of this regional-scale immiscible separation of the Fe-P melts. The produced Fe-P melts would be subsequently equilibrated with fluids (temperature?) which would ascend through the zones of ring fracture (Fig. 2; Förster and Jafarzadeh 1994) and would eventually produce the mineralization at Chador-Malu (and similar parts of the Bafq district). This scenario, however, remains largely speculative, but some geochemical discussion in support of this view is provided below.

REE partitioning between the proposed immiscible phases could produce distinctive chondrite-normalized REE patterns which would provide some indication of the separation condition. The positive Eu anomaly in the Chador-Malu granite (Fig. 12d) versus the negative Eu anomaly in the Chador-Malu iron oxide-apatite deposit (Fig. 12a–c) is the most conspicuous attribute of their REE patterns. Due to the compatibility of divalent Eu in plagioclase and K-feldspar structure, Eu anomalies are predominantly controlled by feldspars, particularly in felsic magmas (Rollinson 1993). Additionally, Eu can exist in both the 2+ and 3+ oxidation states in magmatic systems, depending on the redox potential, which is a function of oxygen fugacity (Henderson 1996). Naslund (1983) documented the exsolution of an iron oxide melt in the $K(Na)AlSi_3O_8$-FeO-Fe_2O_3-SiO_2 system under strongly oxidizing conditions; however, investigating the REE patterns of the immiscible iron oxide globules in the syenitic and alkali rhyolitic xenoliths in the alkali basalts of the Western Carpathians, and comparing them to the REE patterns of the host K-feldspar-bearing rocks, Hurai et al. (1998) interpreted the positive Eu anomalies in the feldspars and the negative Eu anomalies in the conjugate iron oxide melt as an indicator of the magmatic origin of the latter, and concluded that low oxygen fugacity promoted the immiscibility. Likewise, feldspar crystallization and a reducing condition during immiscibility at the Chador-Malu area might have resulted in the generation of Fe-P melts with a negative Eu anomaly which would correspond to the positive Eu anomaly in the Chador-Malu granite (Fig. 12d). Mineralizing fluids equilibrated with the proposed Fe-P melts would have produced the negative Eu anomalies in the Chador-Malu iron oxide-apatite deposit (Fig. 12a–c).

Moreover, Yb and Lu concentrations in the Chador-Malu granite produce an elevated HREE pattern (Fig. 12d). In felsic liquids, accessory phases such as garnet and zircon, may strongly influence a REE pattern, for although they may be present in only small quantities (often much less that 1 % of the rock), their very high partition coefficients mean that they have a disproportionate effect on the whole rock REE pattern. These minerals deplete in HREE so that extreme depletion of HREE relative to LREE is most likely to indicate their presence in the source (Rollinson 1993). Accordingly, the presence of garnet and zircon (documented in the mineral composition of the Chador-Malu granite; Berberian and Berberian 1981) in the silicate magma during immiscibility might have resulted in the generation of Fe-P melts depleted in HREE (relative to LREE), which would correspond to the elevated HREE pattern of the Chador-Malu granite (Fig. 12d). The equilibration of the proposed Fe-P melts with fluids responsible for mineralization would have resulted in the HREE-depleted patterns observed in the Chador-Malu deposit (Fig. 12a–c).

It should be noted that the Zarigan granite, which is associated with certain iron oxide-apatite systems in the Bafq district (Fig. 2), has chondrite-normalized REE patterns very similar to the Chador-Malu granite (Fig. 12d). This suggests that a similar process might have been active in other parts of the Bafq district. The immiscible separation of Fe-P melts can be associated with the mingling of mafic and/or intermediate and felsic magmas (e.g., Clark and Kontak 2004). Although no mafic body has been documented to be present in the Chador-Mau granite, the syn-intrusive character of mafic

bodies in the Narigan granite (Jami 2005) located further south in the Bafq district (Fig. 2) suggests that similar immiscibility models may be plausible in the region.

Features in favor of a metasomatic model

There is abundant evidence for the activity of hydrothermal fluids at Chador-Malu. The main host rocks to the iron orebody (metasomatites; Fig. 4b) have undergone intense actinolitization (Fig. 8a, b). These rocks can be interpreted as highly altered CVSU rhyolites based on the spatial relationship between the two rock units (Fig. 3), absence of linear contacts between them, and microscopic studies which suggest that at least some minerals in the groundmass of the metasomatites (predominantly quartz) are relict magmatic (Fig. 8). The host rock alterations include K-feldsparization (associated with sericitization), albitization, actinolitization (dominant type), and late stage silicic alteration (Fig. 8), which are consistent with the multistage model of alteration in relation with the intrusion of the plutonic bodies of the Bafq district proposed by Daliran et al. (2007). The mentioned host rock alterations are overprinted with a Fe-metasomatism at Chador-Malu (Fig. 8) which is consistent with the generation of Fe-P melts as a late-stage differentiate of magmatism proposed by researchers from both Kiruna and Bafq (Förster and Jafarzadeh 1994; Frietsch and Perdahl 1995).

The northern orebody of the Chador-Malu deposit (this study; Figs. 3 and 4a) is characterized chiefly by massive mineralization style (Fig. 4b) and a cylindrical morphology, and has been interpreted as a Fe-P melt-filled pipe-like diatreme (Jafarzadeh 1981; Förster and Jafarzadeh 1984, 1994); however, these features (i.e., massive orebody cross-cutting the wall rock) may also be described as a product of pervasive metasomatic replacement in the CVSU. Evidence for high-temperature hydrothermal fluids at Chador-Malu includes the intense actinolitization in the host rocks (Fig. 8a, b) and the nucleation of apatite-hosted monazite inclusions (typically occurs at temperatures >700 °C; Harlov et al. 2002; Fig. 11). Another evidence for hydrothermal mineralization is the presence of the breccias consisting of the angular fragments of the metasomatic host rocks cemented by iron oxides as well as the observation of the small ore veins (Fig. 5). The dolomites in the ore zone (Fig. 3) might also suggest that at least part of the rocks replaced by mineralizing fluids were sedimentary rocks of the CVSU. This is consistent with the precipitation of magnetite and apatite in response to the reaction of mineralizing fluids with dolomitic country rocks and changes in pH and Eh proposed by Torab (2008).

The Bafq mining district represents a volcanic field, with extensive activity associated with cauldron subsidence in Early Cambrian (Förster and Jafarzadeh 1994). Hydrothermal media could link the magmatism (and possible Fe-P melt differentiates, see above), through the zones of ring fracture (Fig. 2), to the iron oxide-apatite mineralization at Chador-Malu (and similar parts of the Bafq district). Some evidence for the effects of high-temperature hydrothermal fluids has been presented here; however, further work is required to study the principal source and characteristics of these fluids.

Conclusions

The geology and geochemistry of the Chador-Malu iron oxide-apatite deposit demonstrates its similar characteristics to the Kiruna-type deposits. There is circumstantial evidence for REE mobilization during the leaching of apatite by high-temperature fluids and the associated nucleation of monazite inclusions (Fig. 11). Another evidence for high-temperature fluids at Chador-Malu includes the pervasive replacement of the CVSU rhyolites by actinolite (actinolitization; Fig. 8a, b), which resulted in the formation of the actinolite-rich metasomatic host rocks with a distinctive green appearance (metasomatites; Fig. 4b). The small ore veins and the breccias cemented by iron ore (Fig. 5), as well as the Fe-metasomatism which overprints other types of alteration in the host rock (Fig. 8) support hydrothermal mineralization. Based on the REE geochemistry and spatial relationships, it is proposed that a potential source for metals and P would be late stage Fe-P melt differentiates of the Cambrian magmatism, which is consistent with the late Fe-metasomatism in the host rocks. The proposed Fe-P melts and the mineralization would be linked by hydrothermal media through the zones of ring fracture at Chador-Malu and similar parts of the Bafq district.

Acknowledgments The present study is based on the first author's MSc thesis at Amirkabir University of Technology (Tehran Polytechnic), Tehran, Iran. The authors express their gratitude to the managers of the Chador-Malu Mining and Industrial Co. for access to the deposit, supporting us during field work and sampling, and funding this research. Some costs were also covered by the Amirkabir University of Technology (Tehran Polytechnic) Grant for Graduate Research. This revised version has greatly benefited from the insightful, constructive comments Professor Robert Duncan and other anonymous reviewers kindly provided.

References

Aftabi A, Mohseni S, Babeki A, Azaraien H (2009) Fluid inclusion and stable isotope study of the Esfordi apatite–magnetite deposit, central Iran—a discussion. Econ Geol 104:137–139

Anders E, Grevesse N (1989) Abundances of the elements: meteoritic and solar. Geochim Cosmochim Acta 53:197–214

Barton MD, Johnson DA (1996) Evaporitic source model for igneous-related Fe oxide-(REE-Cu-Au-U) mineralization. Geology 24:259–262

Barton MD, Johnson DA (2000) Alternative brine source for Fe-oxide(-Cu-Au) systems: implications for hydrothermal alteration and metals. In: Porter TM (ed) Hydrothermal iron oxide copper-gold and related deposits: a global perspective, vol 1. PGC Publishing, Adelaide, pp 43–60

Barton MD, Johnson DA (2004) Footprints of Fe-oxide (-Cu-Au) systems. In: Groves DI (ed) SEG 2004: Predictive mineral discovery under cover. Centre for Global Metallogeny, Spec. Pub. 33, The University of Western Australia, pp 112–116

Beaudoin G, Dupuis C, Gosselin P, Jebrak M (2007) Mineral chemistry of iron oxides: application to mineral exploration. In Andrew CJ et al. (eds) Digging Deeper. Proceedings of the 9th Biennial SGA Meeting, Dublin, pp 497-500

Beaudoin G, Dupuis C (2010) Iron-oxide trace element fingerprinting of mineral deposit types. In: Corriveau L, Mumin H (eds) Exploring for Iron Oxide Copper–gold deposits: Canada and global analogues. Geol. Assoc. Canada, pp 111–126

Belousova EA, Griffin WL, O'Reilly SY, Fisher NI (2002) Apatite as an indicator mineral for mineral exploration: trace-element compositions and their relationship to host rock type. J Geochem Explor 76:45–69

Berberian F, Berberian M (1981) Tectono-plutonic episodes in Iran. In Gupta HK, Delany FM (eds) Zagros-Hindu Kush-Himalaya geodynamic evolution, volume 3. American Geophysical Union Geodynamic Series, pp 5-32

Bonyadi Z, Davidson GJ, Mehrabi B, Meffre S, Ghazban F (2011) Significance of apatite REE depletion and monazite inclusions in the brecciated Se–Chahun iron oxide–apatite deposit, Bafq district, Iran: insights from paragenesis and geochemistry. Chem Geol 281: 253–269

Broman C, Nyström JO, Henriquez F, Elfman M (1999) Fluid inclusions in magnetite-apatite ore from a cooling magmatic system at El Laco, Chile. GFF 121:253–267

Clark AH, Kontak DJ (2004) Fe-Ti-P oxide melts generated through magma mixing in the Antauta subvolcanic center, Peru: implications for the origin of nelsonite and iron oxide-dominated hydrothermal deposits. Econ Geol 99:377–395

Daliran F (1990) The magnetite-apatite deposit of Mishdovan, East Central Iran. PhD thesis, Ruprecht-Karls-Universität, Germany

Daliran F (1999) REE geochemistry of Bafg apatites, Iran: implication for the genesis of Kiruna-type iron ores. In: Stanley CJ, Rankin AH, Bondar RJ (eds) Mineral deposits: processes to processing, volume 1. Balkema, Rotterdam, pp 631–634

Daliran F (2002) Kiruna-type iron oxide-apatite ores and apatitites of the Bafq district, Iran, with an emphasis on the REE geochemistry of their apatites. In: Porter TM (ed) Hydrothermal iron oxide copper-gold and related deposits: a global perspective, vol 2. PGC Publishing, Adelaide, pp 303–320

Daliran F, Stosch HG, Williams P (2007) Multistage metasomatism and mineralization at hydrothermal Fe oxide-REE-apatite deposits and "apatitites" of the Bafq District, Central-East Iran. In Andrew C.J. et al. (eds) Digging Deeper. Proceedings of the 9th Biennial SGA Meeting, Dublin, pp 1501-1504

Daliran F, Stosch HG, Williams P, Jamali H, Dorri MB (2010) Early Cambrian iron oxide-apatite-REE (U) deposits of the Bafq district, East-Central Iran. In: Corriveau L, Mumin H (eds) Exploring for Iron Oxide Copper–gold deposits: Canada and global analogues. Geol. Assoc. Canada, pp 147-160

Darvishzadeh A (1983) Esfordi phosphate deposit. Tehran Univ J Sci 13: 2–24 (in Farsi)

Darvishzadeh A, Aletaha-Kohbanani B (1996) Late Precambrian magmatism and tectonomagmatism in Central Iran. Tehran Univ J Sci 22:57–78 (in Farsi with English abstract)

Duncan RJ, Hitzman MW, Nelson EP, Togtokhbayar O (2014) Structural and lithological controls on iron oxide copper-gold deposits of the Southern Selwyn-Mount Dore Corridor, Eastern Fold Belt, Queensland, Australia. Econ Geol 109:419–456

Dupuis C, Beaudoin G (2011) Discriminant diagrams for iron oxide trace element fingerprinting of mineral deposit types. Miner Depos 46: 319–335

Foose MP, McLelland JM (1995) Proterozoic low-Ti iron-oxide deposits in New York and New Jersey: relation to Fe-oxide, Cu-U-Au-rare earth element, deposits and tectonic implications. Geology 23:665–668

Förster HJ, Borumandi H (1971) Jungpräkambrische magnetit-lava und magnetit-tuffe aus dem Zentraliran (Neoprecambrian magnetite lava and magnetite tuffs from the Central Iran). Naturwiss 58:524 (in German)

Förster HJ, Jafarzadeh A (1984) The Chador-Malu iron ore deposit, Bafq district, Central Iran, Magnetite filled pipes. N Jb Geol Paläont (Abh) 168:524–534

Förster H, Jafarzadeh A (1994) The Bafq mining district in Central Iran- a highly mineralized Infracambrian volcanic field. Econ Geol 89: 1697–1721

Frietsch R (1978) The magmatic origin of the iron ores of the Kiruna-type. Econ Geol 73:478–485

Frietsch R (1984) On the magmatic origin of iron ores of the Kiruna-type: a reply. Econ Geol 79:1949–1951

Frietsch R, Perdahl JA (1995) Rare earth elements in apatite and magnetite in Kiruna-type iron ores and some other iron ore types. Ore Geol Rev 9:489–510

Ghorbani M (2013) A summary of geology of Iran. In: Ghorbani M (ed) The economic geology of Iran: mineral deposits and natural resources. Springer Science + Business Media, Dordrecht, pp 45–64

Groves DI, Bierlein FP, Meinert LD, Hitzman MW (2010) Iron oxide copper-gold (IOCG) deposits through Earth history: implications for origin, lithospheric setting, and distinction from other epigenetic iron oxide deposits. Econ Geol 105:641–654

Haghipour A (1974) Étude géologique de la region de Biabanak-Bafg (Iran Central): Pétrographie et tectonique du scole Précambrien et de sa couverture: Unpublished PhD Thesis, Université de Grenoble, France

Harlov DE, Förster HJ (2003) Fluid-induced nucleation of (Y+REE)-phosphate minerals within apatite: Nature and experiment. Part II. Fluorapatite. Am Min 88:1209–1229

Harlov DE, Wirth R, Förster HJ (2005) An experimental study of dissolution-reprecipitation in fluorapatite: fluid infiltration and the formation of monazite. Contrib Miner Pet 150:268–286

Harlov DE, Andersson UB, Förster HJ, Nyström JO, Dulski P, Broman C (2002) Apatite-monazite relations in the Kiirunavaara magnetite-apatite ore, northern Sweden. Chem Geol 191:47–72

Henderson P (1996) The rare earth elements: introduction and review. In: Jones AP, Wall F, Williams CT (eds) Rare earth minerals: chemistry, origin and ore deposits. Chapman & Hall, London, pp 1–19

Henriquez F, Nyström JO (1998) Magnetite bombs at El Laco volcano, Chile. GFF 120:269–271

Hildebrand RS (1986) Kiruna-type deposits: their origin and relationship to intermediate subvolcanic plutons in the Great Bear Magmatic Zone, northwest Canada. Econ Geol 81:640–659

Hitzman MW (2000) Iron oxide-Cu-Au deposits: what, where, when and why. In: Porter TM (ed) Hydrothermal iron oxide copper-gold and related deposits: a global perspective, vol 1. PGC Publishing, Adelaide, pp 9–25

Hitzman MW, Oreskes N, Einaudi MT (1992) Geological characteristics and tectonic setting of Proterozoic iron oxide (Cu-U-Au-REE) deposits. Precambrian Res 58:241–287

Humphris SE (1989) The mobility of the rare earh elements in the crust. In: Henderson P (ed) Rare earth element geochemistry. Elsevier Science Publishers B.V., Amsterdam, pp 317–342

Hurai V, Simon K, Wiechert U, Hoefs J, Konecny P, Huraiova M, Pironon J, Lipka J (1998) Immiscible separation of metalliferous Fe/ Ti-oxide melts from fractionating alkali basalt: P-T-f_{O2} conditions and two-liquid elemental partitioning. Contrib Mineral Petrol 133:12–29

Jafarzadeh A (1981) Die magnetiterzlagerstätte Chadormalu in zentral Iran und ihre exploration (The Chadormalu magnetite ore deposit

in central Iran and its exploration). PhD thesis, Aachen University, Germany, (in German)

Jami M (2005) Geology, geochemistry and evolution of the Esfordi phosphate-iron deposit, Bafq area, Central Iran. Unpublished PhD Thesis, The University of New South Wales, Australia

Jami M, Dunlop AC, Cohen DR (2007) Fluid inclusion and stable isotope study of the Esfordi apatite-magnetite deposit, Central Iran. Econ Geol 102:1111–1128

Jonsson E, Troll VR, H gdahl K, Harris Ch, Weis F, Nilsson KP, Skelton A (2013) Magmatic origin of giant 'Kiruna-type' apatite-iron-oxide ores in Central Sweden. Sci Rep 3:Article No. 1644, DOI:10.1038/srep01644

Loberg BEH, Horndahl AK (1983) Ferride geochemistry of Swedish Precambrian iron ores. Miner Depos 18:487–504

Moghtaderi A, Moore F, Mohammadzadeh A (2007) The application of advanced space-borne thermal emission and reflection (ASTER) radiometer data in the detection of alteration in the Chadormalu paleocrater, Bafq region, Central Iran. J Asian Earth Sci 30:238–252

Mohseni S, Aftabi A (2012) Comment on "Significance of apatite REE depletion and monazite inclusions in the brecciated Sehchahun iron oxide-apatite deposit, Bafq district, Iran: insights from paragenesis and geochemistry" by Bonyadi Z, DavidsonGJ, Mehrabi B, MeffreS, Ghazban F [Chem. Geol. 281, 253–269]. Chem Geol 334:378–381

Mokhtari MAA, Zadeh GH, Emami MH (2013) Genesis of iron-apatite ores in Posht-e-Badam Block (Central Iran) using REE geochemistry. J Earth Syst Sci 122:795–807

Nabatian G, Ghaderi M, Daliran F, Rashidnejad-Omran N (2012) Sorkhe-Dizaj iron oxide–apatite ore deposit in the Cenozoic Alborz-Azarbaijan Magmatic Belt, NW Iran. Resour Geol 63:42–56

Nadoll P, Angerer T, Mauk JL, French D, Walshe J (2012) The chemistry of hydrothermal magnetite: a review. Ore Geol Rev 61:1–32

Naslund HR (1983) The effect of oxygen fugacity on liquid immiscibility in iron-bearing silicate melts. Am J Sci 283:1034–1059

Naslund HR, Aguirre R, Dobbs FM, Henriquez FJ, Nystrom JO (2000) The origin, emplacement, and eruption of ore magmas. IX Congreso Geologico Chileno Actas, Chile, 2:135-139

Naslund HR, Henriquez F, Nystroem JO, Vivallo W, Dobbs FM (2002) Magmatic iron ores and associated mineralisation: examples from the Chilean High Andes and Coastal Cordillera. In: Porter TM (ed) Hydrothermal iron oxide copper-gold and related deposits: a global perspective, vol 2. PGC Publishing, Adelaide, pp 207–226

NISCO (1980) Result of search and valuation works at magnetic anomalies of the Bafq iron ore region during 1976-1979. Unpublished Report, National Iranian Steel Corporation, 260 p

Nyström JO, Henriquez F (1994) Magmatic features of iron ores of the Kiruna type in Chile and Sweden: ore textures and magnetite geochemistry. Econ Geol 89:820–839

Parak T (1975) Kiruna iron ores are not 'intrusive-magmatic ores of the Kiruna type. Econ Geol 70:1242–1258

Philpotts AR (1967) Origin of certain iron-titanium oxide and apatite rocks. Econ Geol 62:303–315

Philpotts AR (1982) Composition of immiscible liquids in volcanic rocks. Contrib Mineral Petrol 80:201–218

Ramezani J, Tucker RD (2003) The Saghand region, Central Iran: U-Pb geochronology, petrogenesis and implications for Gondwana tectonics. Am J Sci 303:622–665

Rhodes AL, Oreskes N (1999) Geology and rare earth element geochemistry of magnetite deposits at El Laco, Chile. Soc Econ Geol Spec Publ 7:299–332

Rollinson HR (1993) Using trace element data. In: Rollinson HR (ed) Using geochemical data. Pearson Education Asia (Pte) Ltd, Singapore (COS), pp 102–170

Sabet-Mobarhan-Talab A (2014) Economic geology and REE geochemistry of the Chador-Malu iron ore deposit. MSc thesis, Amirkabir University of Technology (Tehran Polytechnic), Iran, (in Farsi with English abstract)

Sabet-Mobarhan-Talab A, Alinia F (2014) Mineralogy of the Chador-Malu iron ore deposit: tracking the effects of hydrothermal overprinting. The Conference on Mining Science. Islamic Azad University-Sari Branch, Sari (in Farsi with English abstract)

Samani BA (1988) Metallogeny of the Precambrian in Iran. Precambrian Res 39:85–106

Samani BA (1998) Precambrian metallogenic deposits in central Iran. AEOI Sci Bull 17:1–16 (in Farsi with English abstract)

Shamsi-Pour R, Khakzad A, Rasa I, Vosoughi-Abedini M (2008) Mineralogy and fluid inclusion studies of Chador-Malu iron ore deposit, Bafq, Central Iran. Res J Univ Isfahan 29:129–144 (in Farsi)

Sillitoe RH, Burrows DR (2002) New field evidence bearing on the origin of the El Laco magnetite deposit, northern Chile. Econ Geol 97: 1101–1109

Smith MP, Gleeson SA, Yardley BWD (2013) Hydrothermal fluid evolution and metal transport in the Kiruna District, Sweden: contrasting metal behavior in aqueous and aqueous-carbonic brines. Geochim Cosmochim Acta 102:89–112

Stosch HG, Romer RL, Daliran F, Rhede D (2011) Uranium-lead ages apatite from iron oxide ores of the Bafq District, east-Central Iran. Miner Deposita 46:9–21

Torab F (2008) Geochemistry and metallogeny of magnetite-apatite deposits of the Bafq Mining District, Central Iran. Unpublished PhD Thesis, Clausthal University of Technology, Germany

Torab FM, Lehmann B (2007) Magnetite-apatite deposits of the Bafq district, Central Iran: apatite geochemistry and monazite geochronology. Min Mag 71:347–363

Williams PJ, Barton MD, Fontboté L, de Haller A, Johnson DA, Mark G, Marschik R, Oliver NHS (2005) Iron-oxide-copper-gold deposits: Geology, space-time distribution, and possible modes of origin. Econ Geol 100th Anniversary Volume: 371–406

Williams GJ, Houshmand-Zadeh A (1996) A petrological and genetic study of the Choghart iron ore body and the surrounding rocks. Geol Surv Iran, Tehran, Report, 18 p